Monthly Notices of the ROYAL ASTRONOMICAL SOCIETY

MNRAS **529,** 1917–1940 (2024) https://doi.org/10.1093/mnras/stae255
Advance Access publication 2024 January 23

The *R*-Process Alliance: detailed chemical composition of an *r*-process enhanced star with UV and optical spectroscopy

Shivani P. Shah [1]★ Rana Ezzeddine,[1] Ian U. Roederer,[2,3,4] Terese T. Hansen,[5] Vinicius M. Placco [6] Timothy C. Beers,[4,7] Anna Frebel [4,8] Alexander P. Ji [9,10] Erika M. Holmbeck,[11] Jennifer Marshall[12] and Charli M. Sakari[13]

[1]*Department of Astronomy, University of Florida, 211 Bryant Space Science Center, Gainesville, FL 32601, USA*
[2]*Department of Physics, North Carolina State University, Raleigh, NC 27695, USA*
[3]*Department of Astronomy, University of Michigan, Ann Arbor, MI 48109, USA*
[4]*Joint Institute for Nuclear Astrophysics – Center for the Evolution of the Elements (JINA-CEE), East Lansing, Mi 48824, USA*
[5]*Department of Astronomy, Stockholm University, AlbaNova University Centre, SE-106 91 Stockholm, Sweden*
[6]*NSF's NOIRLab, Tucson, AZ 85719, USA*
[7]*Department of Physics and Astronomy, University of Notre Dame, Notre Dame, IN 46556, USA*
[8]*Department of Physics and Kavli Institute for Astrophysics and Space Research, Massachusetts Institute of Technology, Cambridge, MA 02139, USA*
[9]*Department of Astronomy & Astrophysics, University of Chicago, 5640 S Ellis Avenue, Chicago IL 60637, USA*
[10]*Kavli Institute for Cosmological Physics, University of Chicago, Chicago IL 60637, USA*
[11]*The Observatories of the Carnegie Institution for Science, 813 Santa Barbara St, Pasadena, CA 91101, USA*
[12]*Mitchell Institute for Fundamental Physics and Astronomy and Department of Physics and Astronomy, Texas A&M University, College Station, TX 77843-4242, USA*
[13]*Department of Physics & Astronomy, San Francisco State University, San Francisco CA 94132, USA*

Accepted 2024 January 17. Received 2024 January 14; in original form 2023 December 19

ABSTRACT

We present a detailed chemical-abundance analysis of a highly *r*-process-enhanced (RPE) star, 2MASS J00512646-1053170, using high-resolution spectroscopic observations with *Hubble Space Telescope*/STIS in the UV and Magellan/MIKE in the optical. We determined abundances for 41 elements in total, including 23 *r*-process elements and rarely probed species such as Al II, Ge I, Mo II, Cd I, Os II, Pt I, and Au I. We find that [Ge/Fe] = +0.10, which is an unusually high Ge enhancement for such a metal-poor star and indicates contribution from a production mechanism decoupled from that of Fe. We also find that this star has the highest Cd abundance observed for a metal-poor star to date. We find that the dispersion in the Cd abundances of metal-poor stars can be explained by the correlation of Cd I abundances with the stellar parameters of the stars, indicating the presence of NLTE effects. We also report that this star is now only the sixth star with Au abundance determined. This result, along with abundances of Pt and Os, uphold the case for the extension of the universal *r*-process pattern to the third *r*-process peak and to Au. This study adds to the sparse but growing number of RPE stars with extensive chemical-abundance inventories and highlights the need for not only more abundance determinations of these rarely probed species, but also advances in theoretical NLTE and astrophysical studies to reliably understand the origin of *r*-process elements.

Key words: stars: abundances – stars: chemically peculiar – stars: Population II – ultraviolet: stars.

1 INTRODUCTION

The rapid neutron-capture process (*r*-process) is thought to be responsible for synthesizing about half the isotopes of elements heavier than zinc (atomic number, Z > 30) observed in the Solar System (SS; Burbidge et al. 1957; Cameron 1957), with the slow neutron-capture process (*s*-process) responsible for synthesizing the other half. Easily detected *r*-process elements such as europium (Eu) have also been observed outside the SS, in various Milky Way stars, stellar streams, and dwarf galaxies (e.g. Venn et al. 2004; Ji et al. 2016; Delgado Mena et al. 2017; Marshall et al. 2019; Hansen et al. 2021; Ji et al. 2022, and references therein). However, the primary astrophysical site(s) of *r*-process nucleosynthesis is still unresolved, contributing to a substantial gap in our understanding of Galactic chemical enrichment and evolution (Cowan et al. 2021; National Academies of Sciences & Medicine 2021).

Theoretical studies investigating the properties of *r*-process astrophysical sites have typically relied on the SS *r*-process pattern to understand the range of *r*-process elements synthesized, and the relative quantities in which they are synthesized (e.g. Goriely & Arnould 2001; Schatz et al. 2002; Farouqi et al. 2010; Lippuner et al. 2017; Siegel, Barnes & Metzger 2019; Curtis et al. 2023). However, the SS *r*-process pattern is not directly measured. Instead,

★ E-mail: shivani.shah@ufl.edu

it is obtained as the residual of the SS's total chemical-abundance pattern after accounting for a theoretically derived *s*-process pattern (e.g. Arlandini et al. 1999; Sneden, Cowan & Gallino 2008; Prantzos et al. 2020). In turn, the *s*-process pattern is obtained by calibrating stellar evolution and Galactic chemical-evolution models to the meteoritic abundance of *s*-process-only isotopes, with *s*-process abundances of all other isotopes theoretically inferred (Roederer et al. 2022a). Moreover, the SS *r*-process abundance pattern represents only a single *r*-process template, which is also the result of Galactic chemical evolution over billions of years.

On the other hand, *r*-process-enhanced (RPE) stars serve as more direct and reliable probe of *r*-process nucleosynthesis events, as well as provide the opportunity of obtaining many different *r*-process templates. RPE stars have *r*-process elemental abundances in excess of twice the Fe abundance as compared to the Sun, [Eu/Fe] $> +0.3$[1] (Beers & Christlieb 2005; Holmbeck et al. 2020). RPE stars are typically very metal poor, with [Fe/H] $\lesssim -2.0$, and as a result, they have preserved the pristine chemical fingerprints of very few (in some cases just one) progenitor *r*-process nucleosynthesis events (Frebel 2018, and references therein). Additionally, the heavy-element abundance patterns of the RPE stars originate almost purely from the *r*-process, with minimal contributions from other processes, if any. Given all of this, RPE stars offer a unique view of *r*-process nucleosynthesis in the early Universe.

To fully leverage RPE stars, it is important to determine the abundances for a wide range of their *r*-process elements. Reliable abundances for the rare-earth *r*-process elements ($55 < Z < 71$) can be obtained relatively easily via ground-based optical observations (e.g. Sneden et al. 2009; Gull et al. 2021). On the other hand, to reliably determine abundances for most of the other elements, including lighter elements at and between the first and second *r*-process peaks ($30 < Z < 55$) and heavier elements at and around the third *r*-process peak ($71 \lesssim Z < 84$), supplemental space-based ultraviolet (UV) observations are required (e.g. Siqueira Mello et al. 2013; Roederer et al. 2022a). In fact, robust abundance determinations for some of these elements, such as germanium (Ge, Z = 32), selenium (Se, Z = 33), cadmium (Cd, Z = 48), tellurium (Te, Z = 52), platinum (Pt, Z = 78), and gold (Au, Z = 79), have been possible solely because of UV observations by the *Hubble Space Telescope* (HST; Cowan et al. 1996, 2002; Sneden et al. 1998, 2003; Roederer et al. 2010b, 2014b; Roederer & Lawler 2012a, b; Siqueira Mello et al. 2013).

UV observations of RPE stars are especially desired to characterize the signatures of a larger inventory of *r*-process elements. Signatures of the light *r*-process elements accessible via optical spectra (e.g. Sr, Y, Zr) have indicated that the abundances of these elements deviate from the 'universal' *r*-process pattern observed for the rare-earth and third-peak elements (Sneden et al. 2000; Cowan et al. 2005, 2021; François et al. 2007; Siqueira Mello et al. 2014; Ji et al. 2016; and references therein). The origin of these deviations is still unknown, with different astrophysical sites, conditions, and processes being considered (e.g. Chiappini et al. 2011; Hansen et al. 2012; Wanajo 2013; Holmbeck et al. 2019; Roederer et al. 2022b, 2023). However, the full extent of these deviations is still not even well-established for some elements, such as Se, Cd, and Te, due to their scarce abundances, which require high-resolution UV spectra (Roederer et al. 2022b). The abundances of these elements, especially at and around the second *r*-process peak are also crucial in constraining the effects of nuclear physical processes like fission cycling on the *r*-process abundances (Eichler et al. 2016; Vassh et al. 2019). Similarly, even though the heavier *r*-process elements exhibit a 'universal' abundance pattern, elements such as Pt and Au at the third *r*-process peak have been observed in ∼15 and ∼5 RPE stars, respectively, questioning the extent of the *r*-process universality or alternatively holding undiscovered clues to the still unknown origin of the universality (although see Roederer et al. 2023).

UV observations also offer the opportunity to investigate NLTE effects for the neutral species of elements such as Mg, Al, Co, Ni, Mo, and Os. Specifically, they enable access to the dominant species (usually first ions) of these elements, while their minority species (neutral atoms) are accessible via optical observations (Roederer et al. 2010b, 2022a; Peterson 2011; Roederer & Lawler 2021). A subsequent comparison between the abundances of the dominant and the minority species can promote an empirical assessment of the theoretically predicted NLTE effects for the minority species of the elements, and thereby an assessment of the NLTE models themselves.

However, there are only a few RPE stars that have been analysed with space-based UV observations and ground-based optical observations. These include HD 222 925 (Roederer et al. 2018, 2022a), CS 31082–001 (Cayrel et al. 2001; Hill et al. 2002; Plez et al. 2004; Barbuy et al. 2011; Siqueira Mello et al. 2013), CS 22892–052 (Sneden et al. 2003), HD 108 317 (Roederer et al. 2012a, 2014a, b), BD + 17 3248 (Cowan et al. 2002; Roederer et al. 2010b), HD 160 617 (Roederer & Lawler 2012; Peterson, Barbuy & Spite 2020), HD 84 937 (Peterson, Barbuy & Spite 2020), and HD 19 445 (Peterson, Barbuy & Spite 2020). The scarcity of such studies partly arises from the need of an RPE star to be bright in the NUV (e.g. GALEX *NUV* <15) in order to achieve the necessary signal-to-noise ratio (e.g. Roederer et al. 2022b). Additionally, since the strength of the absorption lines are decreased in such NUV-bright stars due to their higher effective temperatures, the stars also have to be sufficiently *r*-process enhanced to obtain abundances for a wide range of *r*-process elements. Studies of these stars have typically resulted in the determination of ∼25–35 *r*-process elemental abundances for these stars. An exception to this case is HD 222925, for which abundances of a record 42 *r*-process elements were determined. While these studies have already resulted in important theoretical implications for *r*-process-nucleosynthesis (e.g. Roederer et al. 2022b; Holmbeck et al. 2023), further advances in the field are still limited by the small number of stars that are studied in this manner.

In this paper, we present a detailed chemical-abundance analysis of a highly *r*-process-enhanced star, 2MASS J00512646-1053170 (hereafter J0051-1053), using UV observations with the *Space Telescope Imaging Spectrograph* (STIS) on board HST and optical observations with *the Magellan Inamori Kyocera Echelle* (MIKE) instrument at the *Magellan II* telescope. This star is unique from most other RPE stars studied with UV and optical spectroscopy, since it is possibly the warmest star in the sample (∼6400 K) which is also highly *r*-process enhanced ([Eu/Fe] ∼ +1.30) and very low in metallicity ([Fe/H] ∼ −2.30).

This paper is organized as follows: In Section 2, we provide a brief overview of the discovery and previous literature studies of J0051-1053. In Section 3, we describe the data collection and reduction. Stellar parameter determination is outlined in Section 4, while the linelist and atomic data used are specified in Section 5. We describe the abundance determination of all the elements in Section 6. We detail the detection threshold method in Section 7, and the uncertainty analysis in Section 8. We discuss the results in Section 9, and conclude in Section 10.

[1] $[A/B] = \log(N_A/N_B)_{Star} - \log(N_A/N_B)_{Solar}$, where N is the number density of the element.

2 PEDIGREE OF J0051-1053 AND ITS POSSIBLE HELMI STREAM MEMBERSHIP

J0051-1053 was first identified as a candidate metal-poor star by the Hamburg/ESO Survey, and then confirmed to have [Fe/H] = −2.43 through medium-resolution ($R \sim 2000$) spectroscopic followup with the 4-m *Blanco* telescope at the *Cerro Tololo Inter-American Observatory* (Frebel et al. 2006). Subsequently, J0051-1053 was identified as a possible member of the Helmi Stream by Beers et al. (2017). J0051-1053 was then identified by Ezzeddine et al. (2020) as a highly *r*-process-enhanced star with [Eu/Fe] = 1.34 through higher-resolution spectroscopy with *Magellan*/MIKE at the *Las Campanas Observatory*, Chile. Given the importance of its chemical properties as a possible Helmi stream member, J0051-1053 was studied in further detail by Gull et al. (2021), who obtained abundances for 12 *r*-process elements.

We note that a more recent study by Koppelman et al. (2019), who identified ∼600 potential members of the Helmi stream using Gaia DR2 kinematic parameters of over 8 million stars, did not identify J0051-1053 as one of the members. A kinematic analysis of J0051-1053 by G Limberg following the method in Limberg et al. (2021) with updated Gaia DR3 parameters also indicated that J0051-1053 is unlikely to be associated with the Helmi stream (private communication). Given this uncertainty, we do not discuss the membership of J0051-1053 further.

3 DATA ACQUISITION AND REDUCTION

3.1 Optical data

We observed J0051-1053 on 2016 October 14 (MJD = 57675.15855) with Magellan/MIKE (Bernstein et al. 2003) at the Las Campanas Observatory for a total exposure time of 1200s, resulting in S/N of 150 per pixel at 4000 Å. We used the 0.7 arcsec slit with 2 × 2 binning, which yielded a measured resolving power of $R \sim 28\,400/26\,800$ in the blue and red arms, respectively. The blue- and red-arm spectra together cover a wavelength range of 3350–9500 Å. We reduced the spectra of the star using CARPY (Kelson et al. 2000; Kelson 2003), and corrected the radial velocity by cross-correlating against a rest-frame *Magellan*/MIKE spectrum of G 64–12. We determined a resulting heliocentric radial velocity of 56.91 km s^{-1}. To normalize the orders, we used `SMHr`,[2] specifically using a natural cubic spline function with sigma clipping and strong lines masked, which was followed by stitching the orders together to furnish the final spectrum.

3.2 Near-UV data

J0051-1053 was observed with HST/STIS (Kimble et al. 1998; Woodgate et al. 1998) on 2020 January 21, 22, and 23 (Hansen et al. 2019, Proposal ID: 15951). The star was observed with the E230M échelle grating centred at λ2707 Å, providing a wavelength coverage from ∼2275–3119 Å, and with the 0.2 arcsec × 0.2 arcsec slit, providing $R \sim 30\,000$.[3] The observations were made over 12 orbits (i.e. 12 continuous exposures), with three orbits in each visit. The total exposure time over the 12 orbits was ∼5.65 h, resulting in a S/N of 65 at 2707 Å. The spectra were automatically reduced by the CALSTIS software package, and we downloaded the processed spectra from the *Mikulski Archive for Space Telescopes*. We corrected for the radial velocity of each exposure by cross-calibrating a synthetic spectrum of the star generated with `MOOG` (Sneden 1973). We normalized the orders using a natural cubic spline function with sigma clipping, and co-added the normalized orders of all the exposures before stitching to furnish the final spectrum.[4]

4 STELLAR PARAMETERS

We determined the effective temperature ($T_{\rm eff}$) and surface gravity (log g) of J0051-1053 photometrically, based on methods described in Roederer et al. (2018) and Placco et al. (2020). We preferred to use photometric determinations of $T_{\rm eff}$ and log g since spectroscopic determinations based on LTE have been known to be inaccurate and requiring additional corrections (Thévenin & Idiart 1999; Frebel et al. 2013; Ezzeddine, Frebel & Plez 2017; Ezzeddine et al. 2020). Moreover, these methods follow the *R*-Process Alliance convention for homogeneity. We briefly describe the methods used below.

We determined $T_{\rm eff}$ using the colour–[Fe/H]–$T_{\rm eff}$ photometric relations of Casagrande et al. (2010), which require an estimate of the metallicity. We initially used [Fe/H] = −1.97, obtained with spectroscopic determination of the stellar parameters. With new $T_{\rm eff}$ and log g estimates obtained photometrically, we re-determined [Fe/H] using equivalent-width (EW) measurements of Fe I lines in the optical. We repeated the $T_{\rm eff}$ and log g calculation using the photometric relations with [Fe/H] = −2.33.

We calculated $T_{\rm eff}$ from the dereddened V–J, V–H, V– K, and J–K colours. We used the J, H, and K magnitudes from 2MASS (Cutri et al. 2003, Vizier catalog II/246) and the Johnson V magnitude from DR9 of APASS (Henden & Munari 2014, Vizier catalog II/336). We adopted the reddening value, $E(B-V)$, of 0.001 from Schlafly & Finkbeiner (2011) for the line of sight of the star, with the A_λ extinction coefficient for the colour bands from McCall (2004). We chose to not use the $B-V$ colour, because the B-band is sensitive to the CH G-band in carbon-enhanced metal-poor stars, which was not taken into account in the photometric relations. However, as shown below, J0051-1053 was not found to be carbon enhanced. As described in Roederer et al. (2018), we then calculated $T_{\rm eff}$ for each colour band by drawing the input parameters (magnitudes, reddening, and metallicity) 10^4 times from their corresponding error distributions, which we assumed to be Gaussian. We used the median value of the resulting $T_{\rm eff}$ distribution. For the final $T_{\rm eff}$, we used the weighted average of $T_{\rm eff}$ from all the colour bands. For the total uncertainty on $T_{\rm eff}$, we used the uncertainty of the weighted average. As a result, we obtained $T_{\rm eff}$=6440 ± 82 K.

We calculated log g using the following fundamental relation:

$$\log g = 4\log T_{\rm eff} + \log(M/{\rm M}_\odot) - 10.61 + 0.4\cdot(BC_V) + V - 5\log(d). + 5 - 3.1\cdot E(B-V) - M_{\rm bol,\odot} \quad (1)$$

For M, the mass of the star, we assumed 0.8 ± 0.08 M$_\odot$. For BC$_V$, the bolometric correction in the V-band, we used −0.22 (Casagrande & VandenBerg 2014). We obtained the distance d = 264.70 pc from Bailer-Jones et al. (2021). M$_{\rm bol,\odot}$ is the Solar bolometric magnitude, equal to 4.75. We calculated the constant 10.61 from the Solar constants $\log(T_{\rm eff})_\odot = 3.7617$ and $\log g_\odot = 4.438$. We estimated log g by drawing these input parameters 10^4 times from their error distribution and taking the median of the resulting distribution of log g. For the uncertainty on log g, we used the standard deviation of the distribution. We note that, in order to take the error distribution

[2] https://github.com/eholmbeck/smhr-rpa/tree/py38-mpl313

[3] https://hst-docs.stsci.edu/stisihb/chapter-13-spectroscopic-reference-material/13-3-gratings/echelle-grating-e230m

[4] https://github.com/alexji/alexmods/blob/master/alexmods/specutils/continuum.py

of $T_{\rm eff}$ into account as one of the inputs to the log g calculation, we added 150 K in quadrature with the uncertainty calculated above (82 K) to account for other possible systematic uncertainties. This choice has a minimal impact on the log g value. Finally, we obtained log $g = 4.02 \pm 0.07$ dex.

For determining ξ and [Fe/H], we used the EWs of Fe I and Fe II lines, along with the $T_{\rm eff}$ and log g values obtained above. For this, we used `SMHr`,[5] the next-generation spectroscopic analysis tool of `SMH` (Casey 2014). `SMHr` uses the radiative transfer code `MOOG` (Sneden 1973), which we used with the proper treatment of scattering included[6] (Sobeck et al. 2011). For the stellar model atmosphere, we employed the ATLAS9 1D plane parallel LTE grid (Castelli & Kurucz 2003) in `SMHr`. To determine ξ, we minimized the trend in the abundances of the optical Fe I lines and their reduced EWs. We obtained $\xi = 1.59$ km s^{-1}. We assumed a fiducial uncertainty of 0.2 km s^{-1} on ξ. For [Fe/H], we report the resulting mean abundance of the UV and optical Fe II lines, with $T_{\rm eff}$, log g, and ξ fixed to the above values, which is [Fe/H] $= -2.34$. We assumed a fiducial uncertainty of 0.20 dex on [Fe/H] as well.

Given the $T_{\rm eff}$ and log g of J0051-1053, and its position on the Hertzprung–Russell diagram, we identify the star to be near the end of the turn-off phase and at the beginning of the subgiant phase. For the purpose of this paper, we refer to it as a turn-off star.

5 LINELIST AND ATOMIC DATA

We used `linemake`[7] (Placco et al. 2021a, b) to generate the linelists for the UV and optical absorption lines. We specifically used the updated parameters of the CH transitions from Masseron et al. (2014). The linelist included hyperfine splitting structure (HFS) for relevant transitions. Following Roederer et al. (2022a), we included the Au I line at 2376.28 Å, with oscillator strength (log gf-value) from Zhang et al. (2018). We also updated the log gf-values of Hf II lines and included additional Hf II lines from Den Hartog, Lawler & Roederer (2021).

For abundance determination, we investigated absorption lines used by Placco et al. (2015), Roederer et al. (2018), Ji et al. (2020), and Roederer et al. (2022a). We also investigated additional absorption lines of light and heavy elements in the UV from the *National Institute of Standard and Technology Atomic Spectra Database* (NIST ASD; Kramida et al. 2022). We present the final list of absorption lines used for abundance determination in Table A1, along with the corresponding atomic parameters of the lines. We used a total of 113 transitions in the UV and 402 transitions in the optical.

6 CHEMICAL ABUNDANCES

As described in Section 4, we used `SMHr`, along with `MOOG` and ATLAS9 stellar-atmosphere grid, for line-by-line spectral analysis and abundance determination. We determined abundances using EW measurements for Na I, K I, Ca I, Ti II, Fe I, Fe II, and Ni I lines in the optical. For all the other lines, we used spectral synthesis. We used the isotopic ratios of the r-process elements from Sneden, Cowan & Gallino (2008).

For an overview, we present various results of the abundance analysis in tables. Table A1 lists, for all the absorption lines used, the atomic parameters (wavelength, excitation potential, and log gf-value), the abundance determination technique used (EW or spectral synthesis), the resulting abundance, and the systematic uncertainty on the abundance. Table 1 lists the mean abundances of each species from the UV and optical spectra separately, along with the statistical uncertainty. Table 2 lists the adopted abundance for each element, along with the resulting [X/Fe] abundance ratio, the statistical uncertainty, the systematic uncertainty, and the total uncertainty.

In general, we adopted the abundance of the ionized species, if available. If unavailable, we adopted the NLTE-corrected abundance of the neutral species, if the NLTE correction grids were available in the literature. If neither of these cases applied, we adopted the LTE abundance of the neutral species. If available, we generally combined the UV and optical lines for abundance determination of each species by taking the average of all the lines. We further detail the abundance determination for all the elements below.

6.1 Li

We detected a strong Li I absorption feature at 6707.80 Å. We did not detect Li absorption at any other Li I transition lines (e.g. Kowkabany et al. 2022). We used spectral synthesis to fit the λ6707 line and determined log ϵ(Li) = 2.37. This absorption feature has a potential contribution from both the ^{6}Li and ^{7}Li isotopes. We used an isotopic ratio of ^{6}Li/^{7}Li=0.00, since any reasonable isotopic contribution from ^{6}Li is undetectable at the resolution of our spectrum. For instance, increasing the isotopic ratio to 0.01, which is the upper limit suggested by Prantzos (2012) for metal-poor stars based on Galactic chemical evolution, did not change the line profile in any detectable manner. Moreover, it is recommended to implement 3D and NLTE models to reliably constrain the isotopic ratio from the spectral signature (Lind et al. 2013), which is beyond the scope of this work. However, we obtain a NLTE correction of −0.02 using `Breidablik`[8] (Wang et al. 2021), which is an interpolation routine to estimate the NLTE correction of the Li abundance based on the EW of the line. For the final Li abundance, we adopted the NLTE-corrected abundance of log ϵ(Li) = 2.35.

6.2 C and N

We determined log ϵ(C) = 6.70 using the CH G-band at 4313 Å. We also obtained an identical abundance using the C I λ2964.85 line. However, we do not find this line reliable in our spectrum since it is not very well resolved. Moreover, as pointed out by Roederer et al. (2022a), the accuracy of the line's log gf value is graded a D (<50 per cent; ±0.30 dex) by NIST. Therefore, we adopted the C abundance from the CH G-band only. We further considered a correction to the C abundance due to possible CN processing as described in Placco et al. (2014), but find a correction of 0.0 dex[9] due to the relatively early evolutionary stage of the star.

For N, we used the λ3876 CN molecular band. However, the CN absorption features were very weak, so we determined a 3σ upper limit, obtaining log ϵ(N) < 7.73.

6.3 Na, Al, and K

We determined log ϵ(Na) = 3.99 using EW measurements of four Na I lines including the λ5889/λ5895 and λ8183/λ8194 doublets. We

[5] https://github.com/andycasey/smhr
[6] https://github.com/alexji/moog17scat
[7] https://github.com/vmplacco/linemake/tree/ch_masseron
[8] https://github.com/ellawang44/Breidablik
[9] Using the online tool available at http://vplacco.pythonanywhere.com/

Table 1. Mean abundances ($\log \epsilon(X)$), statistical uncertainty ($\sigma_{\rm stat}$), and the number of lines used (N) for each species in the UV and optical (op) domains. Also listed are the NLTE corrections for the mean abundances of each species, UV and optical lines considered together.

Species	$\log \epsilon(X)_{\rm UV}$	$\sigma_{\rm stat,\,UV}$	$N_{\rm UV}$	$\log \epsilon(X)_{\rm op}$	$\sigma_{\rm stat,\,OP}$	$N_{\rm OP}$	$\log \epsilon(X)$	Δ NLTE$_{\rm corr}$
Li I	–	–	–	2.37	0.20	1	2.37	−0.02
O I	–	–	–	7.08	0.05	3	7.08	−0.10
Na I	–	–	–	3.99	0.07	4	3.99	−0.10
Mg I	5.66	0.04	2	5.73	0.09	7	5.72	0.10
Mg II	5.70	0.20	1	–	–	–	5.70	–
Al I	–	–	–	3.32	0.17	2	3.32	0.47
Al II	4.18	0.20	1	–	–	–	4.18	–
Si I	5.58	0.20	1	5.53	0.20	1	5.56	0.00
Si II	5.60	0.01	2	5.47	0.20	1	5.55	–
S I	–	–	–	<5.98	–	1	<5.98	–
K I	–	–	–	3.33	0.20	1	3.33	−0.28
Ca I	–	–	–	4.48	0.09	24	4.48	0.14
Sc II	1.13	0.20	1	1.10	0.05	12	1.10	–
Ti I	–	–	–	3.2	0.10	12	3.2	0.14
Ti II	3.10	0.10	4	3.12	0.15	34	3.12	0.04
V I	–	–	–	2.05	0.2	1	2.05	–
V II	1.99	0.08	6	1.97	0.05	7	1.98	–
Cr I	3.22	0.03	2	3.34	0.05	6	3.31	0.25
Cr II	3.46	0.05	11	3.31	0.02	3	3.43	0.04
Mn I	2.89	0.22	3	2.81	0.02	5	2.84	0.28
Mn II	2.97	0.14	2	2.88	0.07	4	2.91	−0.03
Fe I	5.16	0.11	21	5.19	0.1	156	5.19	0.17
Fe II	5.10	0.12	22	5.23	0.05	14	5.15	0.00
Co I	2.95	0.20	1	2.87	0.12	10	2.88	–
Co II	2.61	0.09	9	–	–	–	2.61	–
Ni I	3.92	0.12	3	3.94	0.16	18	3.94	–
Ni II	3.94	0.04	5	–	–	–	3.94	–
Zn I	–	–	–	2.32	0.02	2	2.32	0.18
Ge I	1.40	0.20	1	–	–	–	1.40	–
As I	<0.84	–	1	–	–	–	<0.84	–
Rb I	–	–	–	<2.42	–	1	<2.42	–
Sr II	–	–	–	1.06	0.08	2	1.06	–
Y II	0.58	0.20	1	0.46	0.13	9	0.48	–
Zr II	1.09	0.09	5	1.15	0.07	10	1.13	–
Nb II	<0.93	–	1	–	–	–	<0.93	–
Mo II	0.75	0.20	1	–	–	–	0.75	–
Ru II	<1.54	–	1	–	–	–	<1.54	–
Rh I	–	–	–	<1.52	–	1	<1.52	–
Pd I	–	–	–	<1.34	–	1	<1.34	–
Ag I	–	–	–	<1.38	–	1	<1.38	–
Cd I	0.63	0.20	1	–	–	–	0.63	–
In II	<0.83	–	1	–	–	–	<0.83	–
Sn I	<2.94	–	1	–	–	–	<2.94	–
Te I	<1.83	–	1	–	–	–	<1.83	–
Ba II	–	–	–	0.48	0.06	5	0.48	–
La II	–	–	–	−0.16	0.06	5	−0.16	–
Ce II	–	–	–	0.24	0.03	2	0.24	–
Pr II	–	–	–	−0.40	0.20	1	−0.40	–
Nd II	–	–	–	0.17	0.12	6	0.17	–
Sm II	–	–	–	0.18	0.2	1	0.18	–
Eu II	–	–	–	−0.46	0.04	5	−0.46	–
Gd II	0.40	0.20	1	0.38	0.04	2	0.38	–
Tb II	–	–	–	<−0.06	–	1	<−0.06	–
Dy II	–	–	–	0.26	0.09	5	0.26	–
Ho II	–	–	–	−0.36	0.11	2	−0.36	–
Er II	–	–	–	0.12	0.19	2	0.12	–
Tm II	–	–	–	−0.67	0.20	1	−0.67	–
Yb II	–	–	–	−0.27	0.20	1	−0.27	–
Lu II	−0.70	0.20	1	–	–	–	−0.70	–
Hf II	–	–	–	<0.67	–	1	<0.67	–
Os II	0.49	0.20	1	–	–	–	0.49	–
Ir I	<1.01	–	1	–	–	–	<1.01	–

Table 1 – *continued*

Species	$\log\epsilon(X)_{UV}$	$\sigma_{stat,\,UV}$	N_{UV}	$\log\epsilon(X)_{op}$	$\sigma_{stat,\,OP}$	N_{OP}	$\log\epsilon(X)$	Δ NLTE$_{corr}$
Pt I	0.60	0.13	2	–	–	–	0.60	–
Au I	−0.06	0.07	2	–	–	–	−0.06	–
Th II	–	–	–	<−0.38	–	1	<−0.38	–
C-H	–	–	–	6.70	0.20	1	6.70	–
C-N	–	–	–	<7.73	–	1	<7.73	–

checked for telluric blending with the λ8183/λ8194 doublet using the telluric spectrum provided with the Arcturus Atlas by Hinkle et al. (2000) and did not identify any strong blending. Moreover, the four Na I sodium lines render abundances in excellent agreement. We also estimated a NLTE correction of −0.10 dex, based on NLTE correction girds provided by Lind et al. (2022). For the final Na abundance, we adopted the NLTE-corrected abundance of $\log\epsilon(\mathrm{Na}) = 4.09$.

For Al, we could determine the abundance for two Al I lines in the optical and one Al II line in the UV using spectral synthesis. For the mean Al I abundance, we obtained $\log\epsilon(\mathrm{Al}) = 3.32$. Specifically, we used spectral synthesis of Al I lines at 3944.00 Å and 3961.52 Å. On the other hand, we determined a much higher abundance of $\log\epsilon(\mathrm{Al}) = 4.21$ using the best-fitting spectral synthesis model for the λ2669.16 Al II line, as shown in Fig. 1 (Roederer & Lawler 2021). The reason for this discrepancy has been proposed to be NLTE effects on the abundances of low-excitation Al I lines, such as those used here, on the order of ∼+0.4 dex for metal-poor main-sequence turn-off stars (Nordlander & Lind 2017; Roederer & Lawler 2021). On the other hand, the ground state λ2669.16 Al II line is considered to be forming in LTE, providing a more faithful Al abundance determination (Mashonkina, Belyaev & Shi 2016; Roederer & Lawler 2021). Indeed, we estimated a NLTE correction of +0.47 dex for Al I based on the NLTE correction grids provided by Mashonkina, Belyaev & Shi (2016). However, in spite of this large NLTE correction, the NLTE corrected Al I is still much lower than the Al II abundance. Therefore, for the final Al abundance, we adopted the Al II abundance of $\log\epsilon(\mathrm{Al}) = 4.21$.

We determined $\log\epsilon(\mathrm{K}) = 3.33$ using EW measurement of the K I line at 7698.96 Å. While we also detected absorption at the λ7664.90 K I line, it appears to be contaminated with telluric blends. We estimated a NLTE correction of −0.28 dex for the K I abundance, based on the NLTE grids provided by Takeda et al. (2002) for the λ7698 K I line. For the final K abundance, we adopted the NLTE-corrected abundance of K I, which was $\log\epsilon(\mathrm{K}) = 3.05$.

6.4 α-Elements: O, Mg, Si, S, and Ca

For O, we determined $\log\epsilon(\mathrm{O}) = 7.08$ using spectral synthesis of the O I triplet near 7770 Å. We also estimated a NLTE correction of −0.10 dex, based on the 1D NLTE correction grids provided by Amarsi et al. (2016a) for the middle O I triplet line in a turn-off star. For the final O abundance, we adopted the NLTE-corrected abundance of $\log\epsilon(\mathrm{O}) = 6.08$.

For Mg, we determined the abundances for seven Mg I lines in the optical, two Mg I lines in the UV, and one Mg II line in the UV, all using spectral synthesis. We obtained $\log\epsilon(\mathrm{Mg}) = 5.73$ and $\log\epsilon(\mathrm{Mg}) = 5.72$, with the optical and UV Mg I lines, respectively. Furthermore, we corrected the mean Mg I abundance from these nine lines for NLTE effects using the Mg I grid provided by Lind et al. (2022). We obtained a correction of + 0.10 dex, bringing the NLTE Mg I abundance to $\log\epsilon(\mathrm{Mg}) = 5.83$. For the Mg II line at λ2828, we obtained $\log\epsilon(\mathrm{Mg}) = 5.70$, in agreement with the LTE as well as the NLTE abundance Mg I abundance. For the final Mg abundance, we adopted the Mg II abundance.

For Si, we determined abundances for Si I and Si II lines in the UV and optical spectra using spectral synthesis. While we detected several Si I lines in the UV spectrum, most were too strong for reliable abundance determination. Aside from the strong lines, two Si I lines at 2438.77 Å and 2443.36 Å yielded Si abundance ∼0.4 dex higher than that determined from other Si I and Si II lines. It is unclear why this is the case, since the excitation potential of these lines, 0.00 and 0.01 eV, respectively, are only slightly lower than that of the other Si I lines investigated, which have excitation potentials in the range of 0.78–1.91 eV. Therefore, we excluded these lines for the purpose of abundance determination, and suggest caution when using these lines. As a result, we used one line from the UV and one from the optical to obtain a mean Si I abundance of $\log\epsilon(\mathrm{Si}) = 5.56$. We also estimated a NLTE correction for the optical Si I line at 3905.53 Å using the MPIA-based NLTE correction tool,[10] which yielded a correction of +0.003 dex based on the NLTE model grids provided by Bergemann et al. (2013). We assume a similar NLTE correction for the UV Si I line and consider +0.003 dex to be the NLTE correction for the mean Si I LTE abundance.

For the mean Si II abundance, we used two Si II lines in the UV and one Si II line in the optical, which yielded $\log\epsilon(\mathrm{Si}) = 5.55$. We find that the Si II abundance is in excellent agreement with the Si I LTE abundance. On the other hand, Roederer, Placco & Beers (2016) and Roederer et al. (2022a) found that the low-excitation Si I lines yielded lower Si abundances than the high-excitation Si I lines and the Si II lines. We suspect that the better agreement observed for J0051-1053 might be in part due to the higher $\log g$ of the star, resulting in lower NLTE effects for the low-excitation Si I lines. For the final Si abundance, we adopted the Si II abundance.

We inspected three S I lines in the λ6700 region (Roederer et al. 2022a), but could not determine a reliable S abundance or upper limit.

We determined the Ca abundance using EW measurements of 24 Ca I lines in the optical and obtained $\log\epsilon(\mathrm{Ca}) = 4.48$. We also included a NLTE correction of +0.26 dex, as computed by Mashonkina, Sitnova & Belyaev (2017) for HD 84937, which has similar stellar parameters as J0051-1053. For the final Ca abundance, we used the NLTE-corrected value of $\log\epsilon(\mathrm{Ca}) = 4.74$.

6.5 Fe-group elements: Sc, Ti, V, Cr, Mn, Fe, Co, Ni, and Zn

We determined the Sc abundance using spectral synthesis of 12 Sc II lines in the optical and one Sc II line in the UV, which yielded $\log\epsilon(\mathrm{Sc}) = 1.10$ and $\log\epsilon(\mathrm{Sc}) = 1.13$, respectively. We used all 13 lines to determine the mean Sc abundance of J0051-1053.

[10] https://nlte.mpia.de/gui-siuAC_secE.php

Table 2. Adopted and recommended abundances for 2MASS J00512646-1053170, along with statistical (σ_{stat}), systematic (σ_{sys}), and total uncertainty (σ_{tot}). The Solar abundances of the elements ($\log\epsilon(X)_\odot$) are taken from Asplund et al. (2009).

Element	$\log\epsilon(X)_\odot$	$\log\epsilon(X)$	[X/Fe]	σ_{stat}	σ_{sys}	σ_{total}
Li	1.05	2.35	+ 3.65	0.20	0.05	0.21
O	8.69	6.98	+ 0.64	0.05	0.05	0.07
Na	6.24	3.89	− 0.00	0.07	0.06	0.09
Mg	7.60	5.7	+ 0.45	0.20	0.08	0.22
Al	6.45	4.18	+ 0.08	0.20	0.06	0.21
Si	7.51	5.55	+ 0.39	0.08	0.05	0.09
S	7.12	<5.98	–	–	–	–
K	5.03	3.05	+ 0.37	0.20	0.05	0.21
Ca	6.34	4.62	+ 0.63	0.09	0.05	0.10
Sc	3.15	1.10	+ 0.30	0.05	0.05	0.07
Ti	4.95	3.12	+ 0.52	0.14	0.07	0.16
V	3.93	1.98	+ 0.40	0.07	0.06	0.09
Cr	5.64	3.43	+ 0.14	0.07	0.07	0.10
Mn	5.43	2.91	− 0.17	0.08	0.05	0.09
Fe	7.50	5.15	+ 0.00	0.12	0.06	0.13
Co	4.99	2.61	−0.03	0.09	0.10	0.14
Ni	6.22	3.94	+ 0.07	0.04	0.09	0.1
Zn	4.56	2.50	+ 0.29	0.02	0.04	0.04
Ge	3.65	1.40	+ 0.10	0.20	0.17	0.26
As	2.30	<0.84	–	–	–	–
Rb	2.52	<2.42	–	–	–	–
Sr	2.87	1.06	+ 0.54	0.08	0.18	0.20
Y	2.21	0.48	+ 0.62	0.13	0.06	0.14
Zr	2.58	1.13	+ 0.90	0.08	0.06	0.10
Nb	1.46	<0.93	–	–	–	–
Mo	1.88	0.75	+ 1.22	0.20	0.05	0.21
Ru	1.75	<1.54	–	–	–	–
Rh	0.91	<1.52	–	–	–	–
Pd	1.57	<1.34	–	–	–	–
Ag	0.94	<1.38	–	–	–	–
Cd	1.71	0.63	+ 1.27	0.20	0.13	0.24
In	0.80	<0.83	–	–	–	–
Sn	0.80	<0.83	–	–	–	–
Te	2.18	<1.83	–	–	–	–
Ba	2.18	0.48	+ 0.65	0.06	0.05	0.08
La	1.10	−0.16	+ 1.09	0.06	0.06	0.09
Ce	1.58	0.24	+ 1.01	0.03	0.05	0.05
Pr	0.72	−0.40	+ 1.23	0.20	0.20	0.28
Nd	1.42	0.17	+ 1.10	0.12	0.11	0.16
Sm	0.96	0.18	+ 1.57	0.20	0.07	0.21
Eu	0.52	−0.46	+ 1.37	0.04	0.05	0.07
Gd	1.07	0.38	+ 1.66	0.03	0.15	0.15
Tb	0.30	<−0.06	–	–	–	–
Dy	1.10	0.26	+ 1.51	0.09	0.09	0.13
Ho	0.48	−0.36	+ 1.51	0.11	0.07	0.13
Er	0.92	0.12	+ 1.55	0.19	0.10	0.21
Tm	0.10	−0.67	+ 1.58	0.20	0.06	0.21
Yb	0.84	−0.27	+ 1.24	0.20	0.05	0.21
Lu	0.10	−0.70	+ 1.55	0.20	0.17	0.26
Hf	0.85	<0.67	–	–	–	–
Os	1.40	0.49	+ 1.44	0.20	0.29	0.35
Ir	1.38	<1.01	–	–	–	–
Pt	1.62	0.60	+ 1.33	0.13	0.13	0.19
Au	0.92	−0.06	+ 1.37	0.07	0.12	0.14
Th	0.02	<−0.38	–	–	–	–
C-H	8.43	6.70	+ 0.62	0.20	0.12	0.23
C-N	7.83	<7.73	–	–	–	–

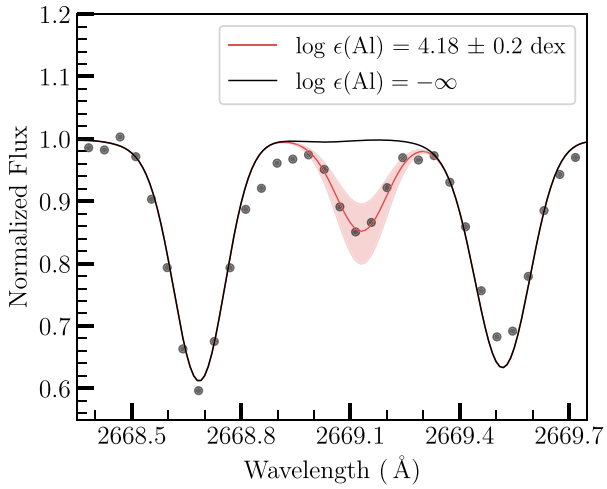

Figure 1. The best-fitting spectral synthesis model for the Al II line at 2669.16 Å is shown with a red-solid line, with the observed data shown in black points. The red-shaded region depicts abundance variation within ±0.2 dex of the best-fitting abundance. The black solid line traces the synthetic model with no contribution from Al.

We determined the Ti abundance using EW measurements of 34 Ti II lines in the optical, which yielded $\log\epsilon(Ti) = 3.12$, and spectral synthesis of five Ti II lines in the UV, which yielded $\log\epsilon(Ti) = 3.10$. We also determined a similar abundance of $\log\epsilon(Ti) = 3.20$ from EW measurements of 12 Ti I lines in the optical. Based on the NLTE analysis of Ti lines in HD 84 937 by Sitnova et al. (2020), we estimated a NLTE correction of +0.14 and +0.04 dex for Ti I and Ti II in J0051-1053, respectively. Given the negligible NLTE effects on Ti II, for the final Ti abundance we adopted the LTE Ti II abundance of $\log\epsilon(Ti) = 3.12$.

We determined the V abundance using spectral synthesis of seven V II lines in the optical and six V II lines in UV, which yielded $\log\epsilon(V) = 1.97$ and $\log\epsilon(V) = 1.99$, respectively. We were also able to determine $\log\epsilon(V) = 2.05$ using the λ4111 V I line, which agrees very well with the V II abundance. We note that NLTE grids for V I and V II are presently not available in the literature. For the final V abundance, we adopted the mean abundance from the 13 V II lines.

For Cr, we determined abundances for Cr I and Cr II lines in the UV and optical spectra with spectral synthesis. We determined $\log\epsilon(Cr) = 3.31$ with Cr I lines and $\log\epsilon(Cr) = 3.42$ using the Cr II line, which agree. We note that the mean Cr II abundance from 11 lines in the UV is +0.15 dex higher than the mean Cr II abundance from three lines in the optical. However, since the discrepancy is on the order of uncertainties on the Cr abundance (∼0.10 dex), we do not suspect anything unusual at play. We also considered a NLTE correction of +0.25 dex and +0.04 dex for Cr I and Cr II, respectively, based on the NLTE analysis of HD 84 937 by Bergemann & Cescutti (2010). Since the NLTE correction for Cr II is negligible, for the final Cr abundance we adopted the mean LTE Cr II abundance from 11 Cr II lines in UV and three Cr II lines in optical, which was $\log\epsilon(Cr) = 3.43$.

For Mn, we determined abundances for Mn I and Mn II lines in the UV and optical spectra. We avoided the triplet Mn I resonance lines in the λ4030 region since these yielded abundances ∼0.20 dex lower than the higher-excitation lines. The systematically lower

abundances obtained with the Mn triplet, relative to other higher-excitation Mn I lines, has been well-documented (e.g. Cayrel et al. 2004; Roederer et al. 2010a; Sneden et al. 2023). We find that the mean Mn II abundance is slightly higher than the mean Mn I abundance, but the discrepancy is within uncertainties. We estimated a NLTE correction of +0.28 and −0.03 dex for the Mn I and Mn II abundances, respectively, based on the NLTE grids provided by Bergemann et al. (2019). For the final Mn abundance, we adopted the mean LTE Mn II abundance of $\log\epsilon(\mathrm{Mn}) = 2.91$ from two UV lines and four optical lines.

For Fe, we determined abundance for Fe I and Fe II lines in the UV using spectral synthesis and for Fe I and Fe II lines in the optical using EW measurements. For Fe I, we determined abundances for 21 lines in the UV and 156 lines in the optical, and obtained a mean Fe I abundance of $\log\epsilon(\mathrm{Fe}) = 5.19$. For Fe II, we determined abundances for 22 lines in the UV and 14 lines in the optical, and obtained a mean Fe II abundance of $\log\epsilon(\mathrm{Fe}) = 5.15$, which agrees very well with the mean Fe I abundance. We note that the mean Fe II abundance with the UV lines is +0.13 higher than the mean Fe II abundance obtained with the optical lines (see Table 1). However, since the standard deviation in the abundances of the UV lines is 0.12, on the same order as the difference in the mean UV and optical abundances, we do not consider this discrepancy to be of concern. We also considered a NLTE correction of +0.17 dex for Fe I and 0.0 dex for Fe II, based on the NLTE analysis of HD 84 937 by Amarsi et al. (2016b). For the final Fe abundance, we adopted the LTE Fe II abundance from the UV and optical lines.

We determined abundances for Co I lines in the UV and optical spectra as well as for Co II lines, which are available only in the UV spectrum. We obtained a significantly higher mean Co I abundance of $\log\epsilon(\mathrm{Co}) = 2.88$ than the mean Co II abundance of $\log\epsilon(\mathrm{Co}) = 2.61$. A similar discrepancy was observed by Cowan et al. (2020) for three other turn-off stars with HST/STIS UV spectra. On the other hand, Roederer et al. (2022a) did not observe such a discrepancy in the giant HD 222925. We further obtained a NLTE correction on the order of +0.89 dex for the Co I lines used here using the Bergemann, Pickering & Gehren (2010) grids,[11] which exacerbates the discrepancy. We note that given the high NLTE corrections obtained and the absence of an explicit analysis of a turn-off metal-poor star in the study, it is unclear whether the grid reliably extends to temperatures as high as 6400 K and metallicity as low as −2.28. We are expecting new NLTE studies for Co in the near future. Nevertheless, we adopted the mean abundance from nine Co II lines in the UV.

We determined abundances for Ni I lines in the UV with spectral synthesis and for Ni I lines in the optical with EW measurements. We also determined abundances for Ni II lines in the UV using spectral synthesis. The mean Ni I abundance of $\log\epsilon(\mathrm{Ni}) = 3.94$ from 18 lines in the optical and three lines in the UV is the same as the Ni II abundance of from 18 lines in the UV, indicating small NLTE effects for Ni I. For the final Ni abundance, we adopted the mean Ni II abundance of $\log\epsilon(\mathrm{Ni}) = 3.94$.

We looked for a Cu I signature at the λ5105 line, however, we could not determine a reliable detection.

Lastly, for this group of elements, we determined $\log\epsilon(\mathrm{Zn}) = 2.32$ with spectral synthesis of two Zn I lines in the optical. We estimated a +0.18 dex NLTE correction on the Zn abundance using the NLTE grids provided by Sitnova et al. (2022) for the λ4810 Zn I line. For the final Zn abundance, we adopted the NLTE-corrected abundance of Zn I, which results in $\log\epsilon(\mathrm{Zn}) = 2.50$.

[11]We used the MPIA NLTE tool online at https://nlte.mpia.de/gui-siuAC_secE.php for interpolating the grids

6.6 Elements at the first *r*-process peak

Of the elements near the first *r*-process peak, including Ga, Ge, As, and Se, the transitions of Ga and Se were out of the spectral range. For Ge, we determined $\log\epsilon(\mathrm{Ge}) = 1.40$ using the λ3039 Ge I line. We show the spectral synthesis fit to the region in Fig. 2. The spectral synthesis fit is not exact, possibly due to noise in the spectrum. Therefore, we assigned an additional 0.10 dex uncertainty for the Ge abundance. For As, we could only determine a 3σ upper limit of $\log\epsilon(\mathrm{As})<0.84$ using the λ2288 As I line.

6.7 Elements between the first and second *r*-process peaks

These elements include Rb (Z = 37), Sr (Z = 38), Y (Z = 39), and Zr (Z = 40). For Rb, we could not detect significant absorption, and thereby determined a 3σ upper limit using the λ7947 Rb I line. For Sr, we determined $\log\epsilon(\mathrm{Sr}) = 1.05$ using two Sr II transitions in the optical. For Y, we obtained $\log\epsilon(\mathrm{Y}) = 0.58$ using one Y II line in the UV and $\log\epsilon(\mathrm{Y}) = 0.46$ using nine Y II lines in the optical. Since the mean UV and the mean optical Y II abundances agree within their statistical uncertainties, we adopted the mean from all 10 lines as the Y abundance. Similarly, we determined the Zr abundance for five Zr II lines in the UV ($\log\epsilon(\mathrm{Zr}) = 1.09$) and 10 Zr II lines in the optical ($\log\epsilon(\mathrm{Zr}) = 1.15$), and we adopted the mean of all 15 lines as the Zr abundance.

For Nb, we detected only a faint absorption signature for the Nb II at 2927.81 Å in the UV. Moreover, the blends were neither resolved nor constrained well by our synthetic spectrum. As a result, we could only determine a 3σ upper limit. For Mo, we determined $\log\epsilon(\mathrm{Mo}) = 0.71$ using the Mo II line at 2871.51 Å in the UV. The other Mo lines were too weak for abundance determination, including the Mo I transitions in the optical. Fig. 2 shows the spectral synthesis fit to the λ2971 line.

We did not detect any clean strong absorption line of Ru I or Ru II in the UV or in the optical. Therefore, we determined a 3σ upper limit for the Ru abundance using the λ2456 Ru II line. Similarly for Rh, we investigated six Rh I lines in the optical, but did not detect a reliable signature for abundance determination. Therefore, we determined a 3σ upper limit for Rh using the λ3435 line. The trend continued for Pd and Ag, for which we could also only determine 3σ upper limits using the λ3405 Pd I and λ3382 Ag I lines. In particular, for the Pd I and Ag I lines, the neighbouring blends were not well-constrained or resolved.

For Cd, we determined $\log\epsilon(\mathrm{Cd}) = 0.63$ with the λ2288 Cd I line. While this line is blended with the λ2288 As I line, the signature of As is negligible in the spectrum of J0051-1053; the Cd-As absorption feature could be fit best by just the Cd abundance. Fig. 2 shows the spectral synthesis fit to the Cd line.

For In, we determined a 3σ upper limit using the In II line at 2306.06 Å. Unfortunately, it is blended with a Fe II line at 2306.17 Å with an uncertain log *gf*-value (Roederer et al. 2022a) and features a very weak absorption signature in the spectrum of J0051-1053. For Sn, we detected a possible signature at the λ2287 Sn I line; however, it was too noisy to yield a reliable abundance or upper limit.

6.8 Second *r*-process peak: Te

The Te I line at 2385.79 Å is not resolved in the spectrum of J0051-1053 and features a very weak absorption signature (see Fig. 2). Furthermore, the neighbouring lines at 2385.59 Å and 2385.92 Å, which are possibly Fe I lines or at least have contribution from them,

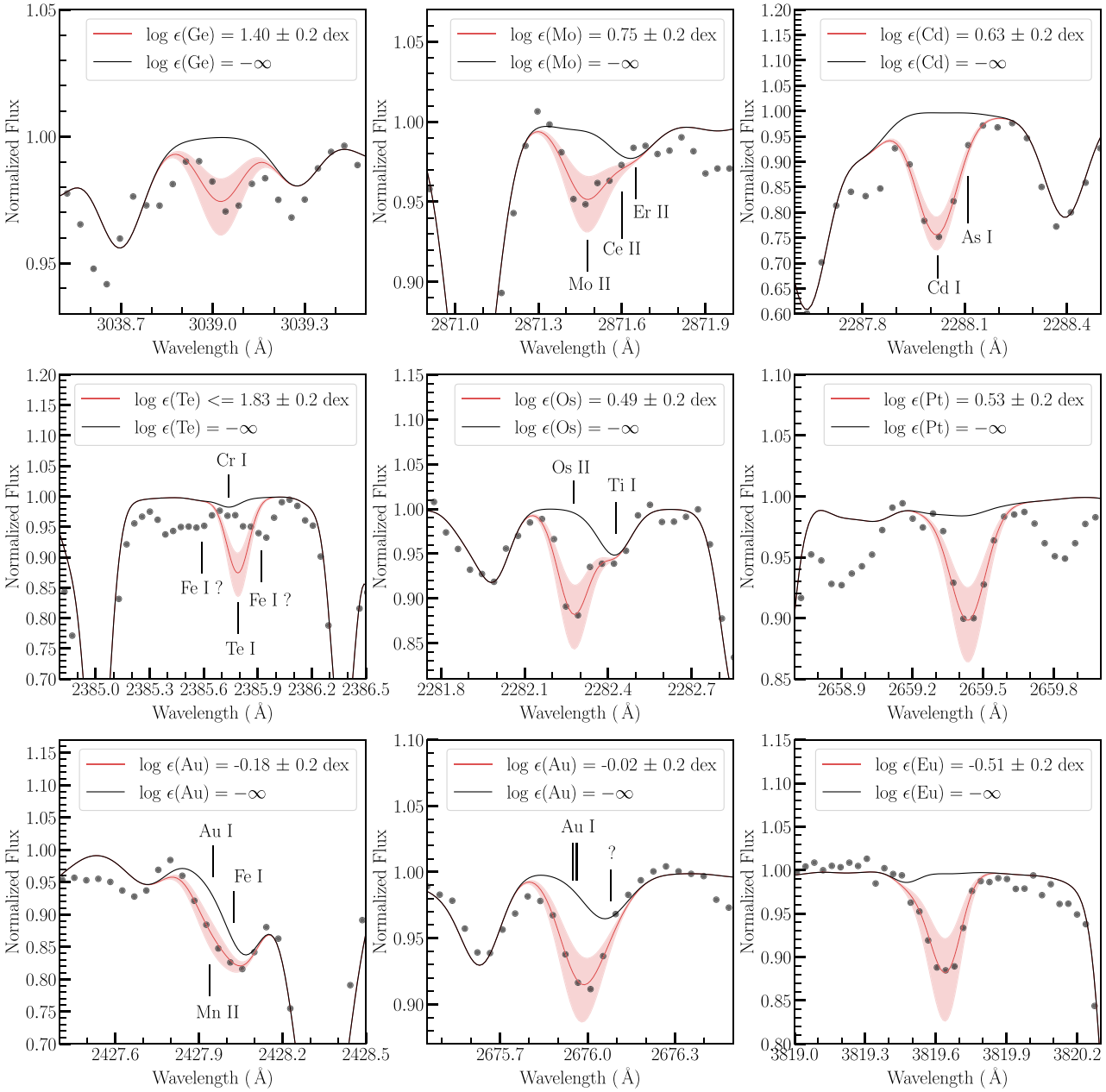

Figure 2. Spectral synthesis fits to absorption lines of various *r*-process elements. The red-solid line traces the best-fitting synthetic model to the observed data in black points. The red-shaded shaded region depicts abundance variation within ±0.2 dex of the best-fitting abundance. The black solid line traces the synthetic model with no contribution from the relevant element. Important neighbouring absorption lines are also labeled.

are not fit well and are blended with the Te I line. There is additional contribution to the Te I feature from a Cr I line at 2385.74 Å. Given the difficulty to reliably constrain the contribution from Te in this spectral region, we determined a 3σ upper limit of $\log \epsilon(\mathrm{Te}) < 1.83$ for the Te abundance. We show the upper limit model for Te in Fig. 2.

6.9 Ba, lanthanides, and Hf

For elements in this group, we determined abundances for all, except for Sm, Tb, and Hf, for which we could only determine upper limits.

For Ba, we used five Ba II transition lines in the optical, which were strong and provided a precise mean abundance. For La, the line strengths were relatively weaker, but five La II transitions were strong enough to obtain reliable abundance determinations. For Ce, we used two Ce II lines to determine the abundance. In general, the other lines were either too weak and/or unresolved, and the contribution from Ce was difficult to constrain. For Pr, we determined the abundance using the Pr II line at 4225.32 Å.

For Nd, we determined the abundance using six Nd II lines in the optical. For Sm, unfortunately, the strongest lines were still weak based on our detection threshold (see Section 7). Therefore, we obtained only a 3σ upper limit on the Sm abundance using the Sm II line at 4329.02 Å. For Eu, we used five Eu II lines in the optical, all of which lend Eu abundance within ±0.10 dex of each other.

For Gd abundance, we used two Gd II lines in the optical and one Gd II line in the UV. All three lines lend Gd abundance within

±0.05 dex of each other. The λ3032 Gd II line in the UV is blended with a Sn I line at 3032.79 Å and a Cr I line at 3029.16 Å. The Cr I line is the dominant source of absorption in this Sn-Gd-Cr feature, but mainly affects the red wing, while the Gd line affects the blue wing. The Sn line is also situated blue and has a direct impact on the Gd abundance. Since the Sn I lines are extremely weak, if not undetectable in the spectrum of J0051-1053, we neglect the Sn contribution to this feature (see Section 6.7). Furthermore, we added an additional ±0.15 dex component to the systematic uncertainty of this line to compensate for the uncertain contribution of Sn.

For Tb, we detected a weak absorption signature at the 3874.17 Å Tb II line, but its signature is below our detection threshold (Section 7). As a result, we determined a 3σ upper limit for the abundance. For Dy, Ho, Er, Tm, and Yb we used five Dy II, two Ho II, two Er II, one Tm II, and one Yb II absorption lines, respectively, in the optical spectrum.

For Lu, we used the Lu II line at 2615.14 Å in the UV spectrum, which displayed a strong signature. The HFS pattern for the line was adopted from Den Hartog, Lawler & Roederer (2020). The Lu II lines in the optical did not display any detectable absorption. While the λ2615 UV Lu II is strong, Roederer et al. (2022b) identified that this line is blended with an unknown transition. They showed that this blend primarily affected stars with low levels of *r*-process enhancement, and would result in an unusually high $\log\epsilon$(Lu/Eu) ratio of $\gtrsim$ 0.5. Since J0051-1053 is highly *r*-process enhanced, with [Eu/Fe] = +1.37, we suspect that the unidentified blend, if present, will have a marginal impact on the Lu abundance. Moreover, upon fitting the Lu feature without accounting for the blend, we obtained $\log\epsilon$(Lu) = −0.70 and $\log\epsilon$(Lu/Eu) = −0.35. Roederer et al. (2022a) determined a similar ratio of $\log\epsilon$(Lu/Eu) = −0.40 for HD 222 925 using other Lu II lines. Nevertheless, for caution, we added an additional ±0.10 dex of systematic uncertainty on the derived Lu abundance.

We checked for several Hf II lines in the UV and optical spectra, but could not determine a reliable absorption signature. Therefore, we determined an upper limit of $\log\epsilon$(Hf) < +0.67.

6.10 Third *r*-process peak: Os, Pt, and Au

We determined the Os abundance using the Os II line at 2282.28 Å in the UV spectrum. The line is situated between an Fe I line at 2281.99 Å and a Ti I line at 2282.43 Å. We adjusted the oscillator strength of these neighbouring lines to fit their lines, but we note that these changes did not impact the fit to the Os line and its derived abundance. We used the log *gf* value for the Os line from Quinet et al. (2006). However, Ivarsson et al. (2004) also provided the log *gf* value for this line, reporting a value lower by ∼−0.10 dex. Therefore, we added a ±0.10 dex systematic uncertainty on the Os abundance from the uncertainty in its log *gf* value.

For Ir, we determined a 3σ upper limit using the Ir I at 2639.71 Å in the UV, since the signature of the line was weak and unresolved.

We determined the Pt abundance using two Pt I lines in the UV at 2659.43 Å and 2997.96 Å. We suspect that there may be an unidentified blend to the λ2997.96 line (see also fig. 4 of Den Hartog et al. 2005), especially since the abundance from this line is higher by 0.15 dex than the abundance from the λ2659.43 line. Therefore, we included an additional ± 0.10 dex systematic uncertainty on this line abundance. The atomic parameters for both the lines, including HFS and IS, were taken from Den Hartog et al. (2005). While we detected absorption signatures at some other Pt I lines listed in Den Hartog et al. (2005), the lines were either not well-resolved or weak.

For the Au abundance, we used the Au I resonance lines at 2427.95 Å and 2675.95 Å. The λ2427.95 line is blended with an Fe II line at 2428.08 Å, which contributes to the red side of the Au-Fe absorption signature, but constrains the data well. The log *gf* value for this Au I line was taken from Hannaford, Larkins & Lowe (1981), with NIST ASD quoting a grade B + (7 per cent, ± 0.05 dex uncertainty). For the λ2676 Au I line, we used the HFS line component provided by Roederer et al. (2022a). The log *gf* value of the line was also taken from Hannaford, Larkins & Lowe (1981), but for this line, NIST ASD quotes a higher accuracy of A + (2 per cent, ± 0.02 dex uncertainty). In our spectrum, this line is primarily blended with an unidentified line. Since the resolution of our spectrum is not high enough to resolve the blend from the Au I line, we used the atomic parameters of this unidentified blend as constrained by Roederer et al. (2022a) for HD 222925. This Au I line is also blended with a Nb II line at 2675.94 Å, for which we estimated a negligible contribution, since the Nb lines in J0051-1053 appear almost undetectable. As a final note, we blue-shifted the wavelength of the λ2676 Au line component by 0.04 Å from the original centre-of-gravity wavelength reported in NIST. The need for a similar wavelength shift was discussed in Roederer et al. (2022a) for HD 222925, but the cause is unclear.

6.11 Actinides

We did not detect any signature of Th or U at any of the Th II and U II lines, including the recently analysed U II lines at 4050.04 Å and 4090.23 Å (Shah et al. 2023). Therefore, we obtained 3σ upper limits for the Th abundance. We do not report the upper limit for U since the spectral regions of the lines were noisy, preventing a constraining upper limit determination.

7 DETECTION THRESHOLD AND UPPER LIMITS

Due to the high temperature of the star, several absorption lines of the *r*-process elements are weak and exhibit absorption depths comparable to the noise level of the spectrum. In order to enable a reliable abundance determination from these weak lines, we employed a minimum EW (EW_{limit}) as the detection threshold. We obtained EW_{limit} using the Cayrel formula for uncertainty on the EW of a weak line (σ_{EW}), as given by equation (2) (Cayrel 1988; Cayrel et al. 2004). Here δx is the width of the pixel in Å, which is ∼0.04 Å for both the UV and optical spectrum. We then obtained EW_{limit} as $2\sigma_{EW}$, as shown in equation (3).

$$\sigma_{EW} = \frac{1.5}{S/N}\sqrt{FWHM * \delta x} \quad (2)$$

$$EW_{limit} = 2\sigma_{EW} \quad (3)$$

With this method, the EW_{limit} is 1.6 mÅ for the optical spectrum and 3.8 mÅ for the UV spectrum. Therefore, we only use lines that have EWs, as obtained from the best-fitting spectral synthesis model, larger than the EW_{limit} of the respective spectrum. In general, most of the weak lines used for abundance determination have EWs larger than $3\sigma_{EW}$. One notable exception is the λ3039 Ge I line, which has an EW measurement of $2.1\sigma_{EW}$. We further discuss the abundance determination with this line in Section 9.2.1. In addition to this detection threshold, we take into account unknown blends and the overall fit to the spectral region when using a line for abundance determination.

For elements that did not have any lines with signatures beyond the detection threshold, we determined a 3σ upper limit on the

element abundance with a suitable line of the element. The most suitable line for upper-limit determination was chosen based on the strength of the line, the S/N in the spectral region, and the constraint on the neighbouring lines. Specifically, the 3σ upper limit was obtained such that the least χ^2 value of the upper-limit spectral-synthesis model was higher than the least χ^2 value of the best-fitting spectral-synthesis model by 3σ, where σ is the spectral noise of the data.

8 UNCERTAINTY ANALYSIS

To determine the total uncertainty (σ_{tot}) for the abundance of an element, we took into account statistical uncertainties (σ_{stat}), which represented uncertainties in the determination of the atomic parameters of the lines, and systematic uncertainties (σ_{sys}), which represented uncertainties in the stellar parameters and line fits. These are listed in Table 2. We added the σ_{stat} and σ_{sys} uncertainties in quadrature to obtain σ_{tot}.

For σ_{stat}, we used the standard deviation in the abundances from individual lines, in the cases six or more lines were used ($N \geq 6$). In case, $2 \leq N \leq 5$, we obtained σ_{stat} by multiplying the range of the abundances with the k-factor from Keeping (1962), to compensate for the small samples and obtain more realistic uncertainty estimates (e.g. Cain et al. 2018). In the case $N = 1$, we assigned a fiducial uncertainty of ± 0.20 dex to σ_{stat}.

For σ_{sys}, we accounted for uncertainties from stellar parameters, T_{eff}, log g, ξ, and [Fe/H] and additional uncertainties from spectral-synthesis fitting due to blends, uncertain atomic parameters, or uncertain continuum placement (see Section 6 for details). We first obtained σ_{sys} for each line and then took their average to represent the systematic uncertainty on the mean abundance of the element, which we list in Table 2. To obtain the uncertainties from the stellar parameters, we individually changed T_{eff}, log g, ξ, and [Fe/H] by ± 82 K, ± 0.07 dex, ± 0.2 km s^{-1}, and ± 0.2 dex, respectively. We added the uncertainties from each of the stellar parameters as well as the uncertainty from the spectral models in quadrature to obtain σ_{sys} for each line.

9 DISCUSSION

9.1 Light elements

Among the light elements with Z $\leq$ 30, we obtained abundances for 16 elements, including 26 species. In the following sections, we discuss the abundances from the UV and optical lines (Section 9.1.1), the observed NLTE effects and theoretical corrections (Section 9.1.2), and the adopted abundances of J0051-1053 compared to that of other metal-poor stars from Roederer et al. (2014a) (Section 9.1.3).

9.1.1 UV and optical abundances

The UV spectral coverage enabled us to determine abundances of four unique species, which are generally not detectable in the optical spectra, including Mg II, Al II, Co II, and Ni II. Additionally, since these are the dominant species, their detection enabled an empirical test of the NLTE effects affecting the corresponding neutral species of these elements (see Section 9.1.2).

The UV spectral coverage also benefited the abundance determinations of 14 species by increasing the number of absorption lines available. These species included Mg I, Si I, Si II, Sc II, Ti II, V II, Cr I, Cr II, Mn I, Mn II, Fe I, Fe II, Co I, and Ni I. We find that the optical and UV abundances of these species agree well, within uncertainties. This can be seen in the top panel of Fig. 3, which shows the individual optical (black data points) and UV (green data points) [X/Fe] abundance ratio of each species. The agreement in the UV and optical abundances of these species validates our reduction and analysis techniques for the two spectra (e.g. Roederer et al. 2022b).

On the other hand, optical spectral coverage enabled us to determine abundances for eight species which were not available in the UV, including O I, Na I, Al I, K I, Ca I, Ti I, V I, and Zn I.

9.1.2 Neutrals, ions, and NLTE effects

We obtained abundances of both the neutral and first-ionized species for several light elements. We plot these abundances as [X/Fe] abundance ratio in the middle panel of Fig. 3, with square data points for neutral species and circular data points for first-ionized species. For this plot, we combined the UV and optical abundances of the species; both the UV and optical lines are considered for the mean [X/Fe] abundance ratio and the corresponding uncertainty of the species following the method described in Section 8. We also depict the LTE and NLTE-corrected abundances for each species separately, coloured-coded with black and red data points, respectively.

As seen in Fig. 3, the abundances of the neutral and ionized species of most light elements agree. On the other hand, for HD 222925, Roederer et al. (2022a) observed that the abundances of the neutral species of Ca and Fe-group elements were all systematically lower than the abundances of their ionized counterparts. They noted that these offsets were consistent with over-ionization effects predicted for these species due to LTE assumptions. Given the higher log g of J0051-1053, we suspect that the over-ionization effects are lower in this case and/or the precision of the abundances derived here is not sufficient to discern any systematic offset between the abundances of the neutral and ionized species.

We also find that the NLTE-corrected abundances of the neutral species (red-square points in the middle panel of Fig. 3) generally agree well with the LTE abundances of the corresponding ionized species (black circular points). The agreement is very good for Mg and Si. In the cases of Mg I and Si I, the NLTE corrections are also small i.e. +0.10 dex and +0.00 dex, respectively. For Ti, Cr, Mn, and Fe, the agreement exists within uncertainties. We note that the NLTE corrections for Cr I (+0.25 dex), Mn I (+0.28 dex), and Fe I (+0.17 dex) are at least 1σ higher than their respective uncertainties. Such significant corrections highlight the importance of NLTE studies and accounting for NLTE corrections as we move towards larger and and more precise spectroscopic surveys and analyses. Overall, the general agreement between the NLTE-corrected abundances of the neutral species and the LTE abundances of the corresponding ionized species, in spite of the large corrections, reflects well on the current state of NLTE theoretical models for most species. Although, as spectroscopic studies start achieving higher precision in the abundances, discrepancies might be revealed.

An important exception to this case is Al, wherein the NLTE-corrected abundance of Al I and the LTE abundance of Al II are discrepant by $\sim$0.4 dex. The NLTE correction for the λ3961 Al I resonance line is significant and is estimated to be +0.47 dex by Mashonkina, Belyaev & Shi (2016). We also used the NLTE grids from Nordlander & Lind (2017),[12] to obtain a similar correction of +0.49 dex. Other NLTE studies, such as Lind et al. (2022),

[12] https://www.mso.anu.edu.au/~thomasn/NLTE/data/

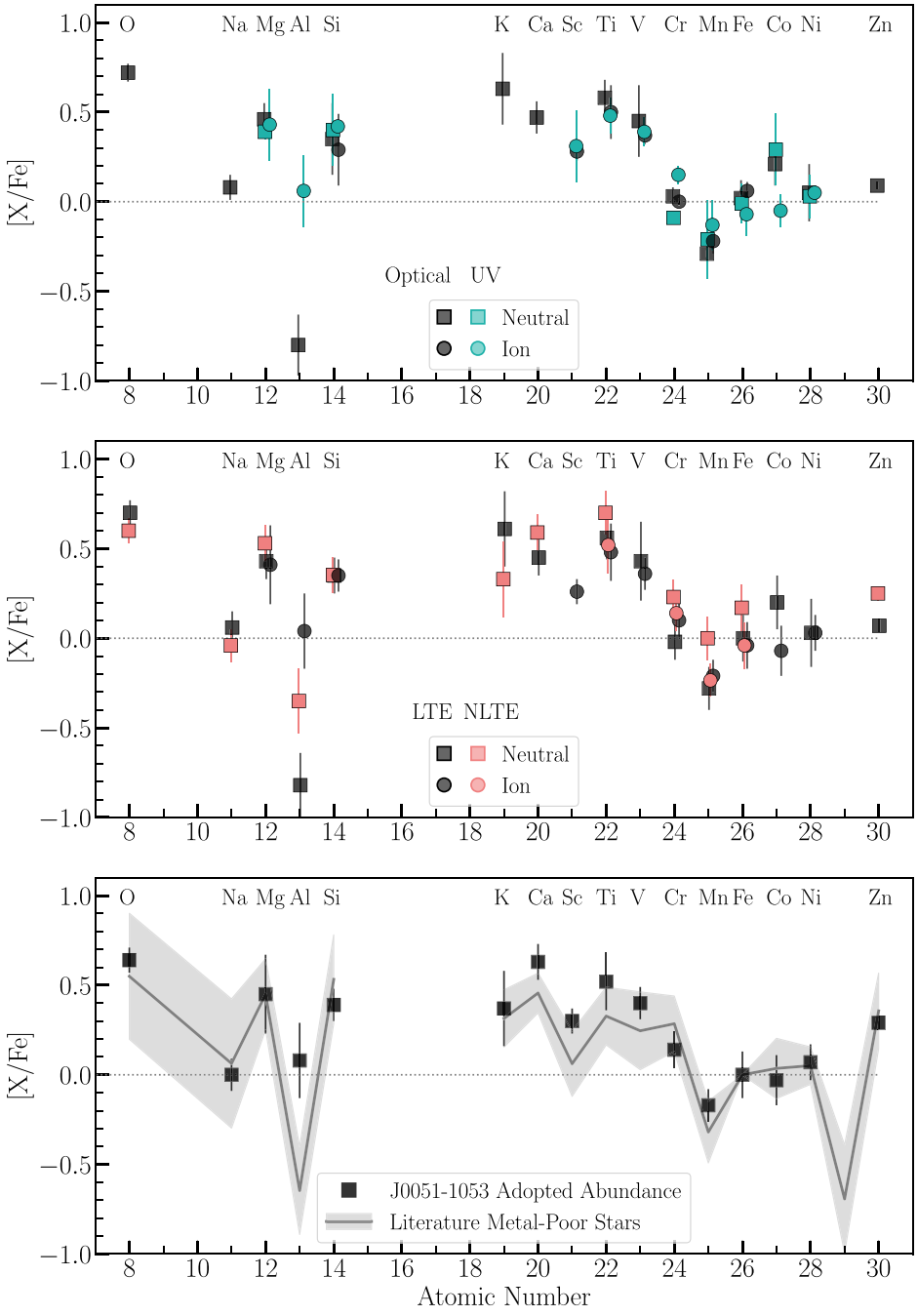

Figure 3. Top Panel: Mean [X/Fe] abundances of light-element species from the UV (green points) and optical spectra (black points). Middle Panel: Mean LTE (black points) and NLTE-corrected (red points) abundances of light-element species. Bottom Panel: The adopted abundances of the light elements for J0051-1053 are shown with black-square points. The black solid line traces the mean [X/Fe] abundances of these elements for the metal-poor stars analysed in Roederer et al. (2014a). The grey-shaded region traces the corresponding standard deviation in the [X/Fe] abundances for the Roederer et al. (2014a) sample.

suggest even smaller NLTE corrections for Al I, on the order of ∼0.20 dex. Interestingly, even with this significant correction, the NLTE-corrected abundance of Al I using the λ3944 and λ3961 resonance lines is still ∼0.40 dex smaller than the Al II LTE abundance with the λ2669 line. Moreover, Mashonkina, Belyaev & Shi (2016) and Nordlander & Lind (2017) showed that NLTE effects for Al II are negligible. Therefore, for this study we adopted the Al II abundance. However, we recommend future NLTE studies to to investigate the source of this discrepancy.

As noted in Section 6, for Li, O, Na, K, Ca, and Zn, we adopted the NLTE-corrected abundance of the neutral species (red square points in the middle panel of Fig. 3), since the abundances of their ionized species were not available. The NLTE corrections for some of these elements are significant e.g. −0.28 dex for K I, +0.14 dex for Ca I, and +0.18 dex for Zn I (also see Table 1), indicating that it is especially important to take NLTE corrections into account for these elements, since their ionized species are generally not available. On the other hand, we note that the analysis of Zn I and Zn II abundances

by Roederer & Barklem (2018) for metal-poor dwarf and subgiant stars indicated minimal ($\lesssim 0.10$ dex) departures from LTE.

9.1.3 Comparison to Other Metal-Poor Stars

We show the adopted light-element abundances of J0051-1053 in the bottom panel of Fig. 3 with black data points and in the form of [X/Fe] abundance ratios. For comparison, we also display the typical values and range of the [X/Fe] abundance ratios for metal-poor stars. For this purpose, we used the light-element abundance ratios of 247 stars, as part of a sample of 313 stars analysed by Roederer et al. (2014a). We obtained the abundances using `JINAbase`[13] (Abohalima & Frebel 2018). Specifically, we show the mean [X/Fe] abundance ratios of this sample with a grey-solid line and the ± 1 standard deviation from the mean with a shaded grey region. As seen in the figure, we have obtained abundances of several light elements for J0051-1053.

The resulting [X/Fe] abundance ratios of J0051-1053 generally compare well with that of the metal-poor stars in the Roederer et al. (2014a) sample. Some discrepancies include [Al/Fe] and potentially [Ca/Fe], due to inconsistency in the adopted values. For [Al/Fe], we adopted the Al II abundance, which is much higher than the Al I abundance due to NLTE effects (see Section 9.1.2), whereas Roederer et al. (2014a) adopted the Al I abundance. Similarly, for [Ca/Fe], we adopted the NLTE-corrected Ca I abundance, while Roederer et al. (2014a) adopted the LTE Ca I abundance, which is generally slightly lower. We note that for O I, Na I, and K I, the NLTE-corrected abundances were adopted by both this study and Roederer et al. (2014a). Our final note is that for Ti, V, Cr, and Mn, both this study and Roederer et al. (2014a) adopted the abundance of the ionized species; on the other hand, for Mg, Si, and Co, we adopted the abundance of the ionized species and Roederer et al. (2014a) adopted the abundance of the neutral species, but no difference is observed in the abundance ratios

In general, the trends in the light-element abundances of J0051-1053 compare well with that of other metal-poor stars, indicating that the primary enrichment channel for the light elements of J0051-1053 was core-collapse supernovae. We obtained an α-enhancement of $[\alpha/\mathrm{Fe}] = +0.42$ for J0051-1053, using abundances of O, Na, Mg, Si, and Ca, which is typical of metal-poor stars (Roederer et al. 2014a; Cowan et al. 2020). We included Ti as an iron-group element here, given the discussions in Curtis et al. (2019) and Cowan et al. (2020). The iron-group elements also exhibit the typical trends, including enhancement of Sc, Ti, and V, followed by solar ratios for Cr, Co, and Ni, followed by some enhancement for Zn (Cowan et al. 2020; Sneden et al. 2023).

The elemental abundances not shown in Fig. 3 are Li and CH. The Li abundance of $\log \epsilon(\mathrm{Li}) = 2.35$, including the NLTE correction, falls along the Spite Plateau (Spite & Spite 1982; Norris et al. 2023), which is expected for a turn-off star. Finally, with $[\mathrm{C/Fe}] = +0.62$, using the CH abundance, we confirm that the star is not carbon enhanced. All in all, we determined abundances for 16 elements and one molecule (CH), and a 3σ upper limit for one element (S) and one molecule (CN).

9.2 Heavy elements and the *r*-process pattern

We obtained abundances for 23 *r*-process elements with $31 \leq Z \leq 92$. Out of these 23 elements, we obtained abundances of eight elements with the UV spectrum and three elements with both the UV and optical spectrum. We also obtained 3σ upper limits on the abundances of 13 *r*-process elements. The UV spectrum especially enabled the upper limit determination for six of these elements.

We show the final abundances of all the neutron-capture elements in Fig. 4. Given the *r*-process enhancement of the star as determined by $[\mathrm{Eu/Fe}] = +1.37$ and $[\mathrm{Ba/Eu}] = -0.72$ (Beers & Christlieb 2005; Frebel 2018), we confirm the findings of other studies (Ezzeddine et al. 2020; Gull et al. 2021) that J0051-1053 is an *r*-II star i.e. a highly RPE star with $[\mathrm{Eu/Fe}] > +0.7$. This classification is further affirmed by the abundance pattern of the neutron-capture elements, which generally matches the SS *r*-process pattern, as seen in Fig. 4. Here the SS *r*-process pattern is scaled to the *r*-process pattern of J0051-1053 using the mean lanthanide abundance. For the mean lanthanide abundance, we specifically used abundances of elements from Ba to Hf, except for Sm and Tb, since we only have upper limits on their abundances. For comparison, we also show the abundance pattern of HD 222925, a metal-poor *r*-II star with abundances of 42 *r*-process elements determined by Roederer et al. (2018, 2022a). We note that the data points for J0051-1053 in the Fig. 4 are colour-coded based on the origin of the abundance of the elements from the UV spectrum (blue), optical (red), or both (yellow). We further discuss the *r*-process pattern of J0051-1053 and compare it to the SS and HD 222 925 *r*-process patterns below.

9.2.1 R*-process pattern from the first to the second* r*-process peak*

Various studies have indicated that the abundance pattern of the elements in this region (from Z = 31 to Z = 52) have a scatter and deviate from the SS *r*-process pattern, even in RPE stars (e.g. Siqueira Mello et al. 2014; Ji et al. 2016). The origin of this effect is still unknown, with different astrophysical sites, conditions, and processes being considered (e.g. Chiappini et al. 2011; Hansen et al. 2012; Wanajo 2013; Holmbeck et al. 2019). For J0051-1053, we also observe the Ge and Y abundances to be lower than the scaled SS *r*-process pattern (see Fig. 4). Additionally, the upper limit on the As abundance is also significantly lower than the scaled SS *r*-process pattern. On the other hand, we observe the Sr, Zr, Mo, and Cd abundances to follow the scaled SS *r*-process pattern.

In the case of Ge, we find that its abundance ratio of $[\mathrm{Ge/Fe}] = +0.10$ is significantly higher than observed in $\sim$20 metal-poor stars so far, which have a mean [Ge/Fe] of ~ -0.90 with a standard deviation of $\sim$0.26, indicating a difference in the origin (Cowan et al. 2005; Roederer et al. 2014b; Peterson, Barbuy & Spite 2020, and references therein). Cowan et al. (2005) showed that for metal-poor stars, [Ge/H] ratio is correlated with [Fe/H], pointing to a common origin of Ge and Fe-peak elements, possibly α-rich freezeout in core-collapse supernovae (also see Roederer et al. 2014b for a similar discussion and larger sample of abundances). However, other mechanisms are also capable of producing Ge, including the *νp*-process (e.g. Fröhlich et al. 2006) and the *r*-process (e.g. Farouqi et al. 2010), both of which have multiple potential astrophysical sites. Therefore, the high [Ge/Fe] ratio observed here may indicate a production mechanism of Ge decoupled from that of Fe. As noted by Roederer et al. (2014b), it will be challenging to establish the originating mechanism without the isotopic abundances. Nevertheless, this result renews the need for more Ge abundance determinations in metal-poor stars. We also consider that the Ge abundance derived here may not be dependable, since only one Ge I line was used. Additionally, there could be NLTE effects present. Therefore, caution is warranted before over-interpreting this Ge abundance.

[13] https://jinabase.pythonanywhere.com/index

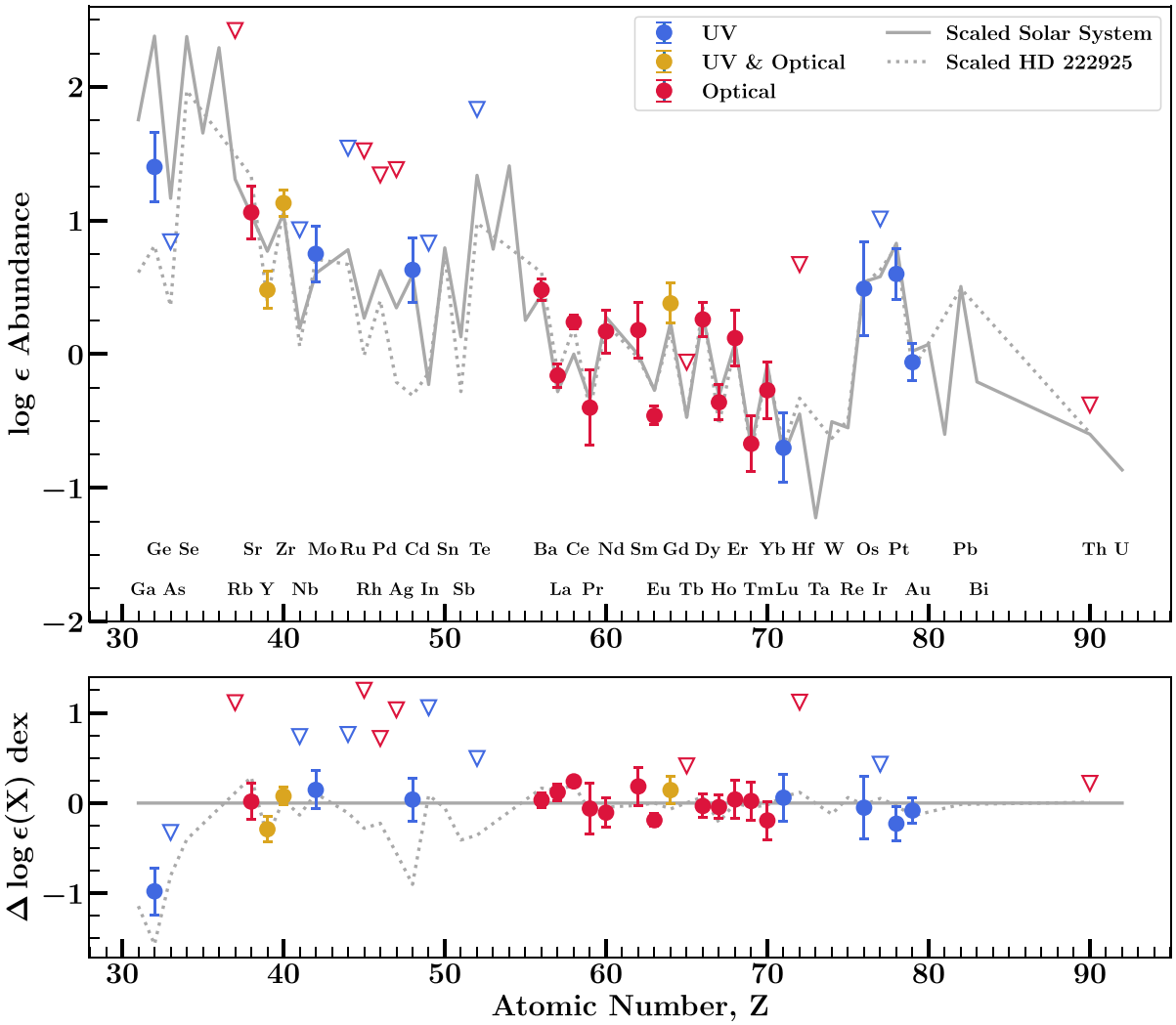

Figure 4. Adopted abundances of the *r*-process elements for J0051-1053 shown with different coloured data points, depending on the wavelength-region used for deriving the abundance. Abundances obtained with the UV spectrum are shown in blue, with optical spectrum are shown in red, and with both UV and optical are shown in yellow. Upper limits are shown in downward-triangle with the same colour map as the abundances. The grey-solid trace depicts the scaled SS *r*-process pattern as obtained from Prantzos et al. (2020). The grey dotted line depicts the scaled *r*-process pattern of the RPE star, HD 222925, as obtained from Roederer et al. (2022a).

Interestingly, in a recent study, Roederer et al. (2022b) showed using eight metal-poor stars, including six RPE, that the relative abundances of Se, Sr, Y, Zr, Nb, Mo, and Te in these stars actually all agree, provided that the abundances are scaled by a light *r*-process element. We find J0051-1053 to conform to this rule based on the derived abundances of Sr, Y, Zr, and Mo. We show this agreement in Fig. 5, where we have plotted the Zr-scaled abundances of the Roederer et al. (2022b) sample stars with grey data points, and the Zr-scaled abundances of J0051-1053 with black data points. We also show the Zr-scaled *r*-process pattern of the SS from Prantzos et al. (2020) with a grey-solid line. Additionally, although we only have 3σ upper limits for Nb and Te for J0051-1053, they do not rule out a possible agreement with other metal-poor stars. In fact, we note that the expected Te abundance, based on the Zr-scaled SS *r*-process pattern lends a stronger absorption signature for the Te I line than the observed data suggests, indicating that the Zr-scaled Te abundance for J0051-1053 is not as high as the Zr-scaled SS Te abundance. On the other hand, the expected Te abundance, based on the Zr-scaled Te abundance of HD 222 925 is more likely to be a better fit to the observed data. Therefore, our current results for J0051-1053 supports the hypothesis proposed by Roederer et al. (2022b) that the enrichment source of the light *r*-process elements in the early Universe must have been common and consistent in producing the observed relative abundances of these elements.

We note here that several studies have pointed out the significant deviation of Y in metal-poor stars from the scaled SS *r*-process pattern (e.g. Sneden et al. 2003; Roederer et al. 2022b), as can be seen in Figs 4 and 5. In a recent study, Storm & Bergemann (2023) computed NLTE departure coefficients for the low- and high-excitation Y II lines for a range of stellar parameters and found that these corrections can be as large as +0.50 dex for low-excitation Y II lines in metal-poor red-giant stars. For a metal-poor turn-off star, they calculated NLTE corrections on the order of ∼+0.15 dex for the low-excitation Y II lines. They proposed that such NLTE effects could contribute to the observed deviation of Y abundances from the SS *r*-process pattern. Indeed, we find that taking into account a +0.15

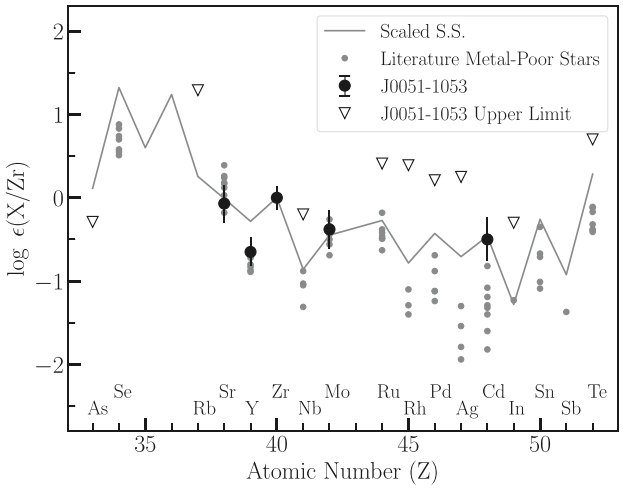

Figure 5. Light *r*-process elements of metal-poor stars scaled to Zr. As identified by Roederer et al. (2022b), abundances for Se, Sr, Y, Zr, Nb, Mo, and Te show minimal dispersion for the eight metal-poor stars in their sample (grey data points). The SS *r*-process scaled to Zr is shown with a grey-solid line. We note that the scaled Sr, Y, and Mo abundances of J0051-1053 (black data points) follow the trend of other metal-poor stars. On the other hand, the scaled Cd abundance of J0051-1053 is much higher, the highest observed in metal-poor stars so far, adding to the observed dispersion of Cd abundances in metal-poor stars.

dex of NLTE effects for the low-excitation Y II lines used here would enable an agreement between the lanthanide-scaled Y abundance of J0051-1053 and the SS *r*-process pattern within uncertainties.

As seen in Fig. 5, we note that an agreement in the relative abundances of the light *r*-process elements in metal-poor stars does not extend to Ru, Rh, Pd, Ag, Cd, and Sn. Of these elements, for J0051-1053, we have abundance determined for Cd and 3σ upper limits determined for Ru, Rh, Pd, and Ag. We find that J0051-1053 has the highest reported $\log\epsilon$(Cd), $\log\epsilon$(Cd/Zr) and $\log\epsilon$(Cd/Eu) abundance among the nine metal-poor stars with Cd abundance determined so far (Roederer et al. 2010b, 2014b, 2022a; Peterson, Barbuy & Spite 2020). This record-high abundance further contributes to the large dispersion in the $\log\epsilon$(Cd/Zr) abundance ratio of metal-poor stars, as seen in Fig. 5. Note that we have not included the Cd abundance of HD 196 944 from Placco et al. (2015) in Fig. 5, since its chemical composition mainly originates from the *s*-process.

While the production of Cd has not been of specific focus due to the small number of observations, theoretical studies have indicated that elements in this region ($44 < Z < 51$) could be formed through the weak *r*-process i.e. a neutron-capture process with intermediate neutron densities (e.g. Montes et al. 2007). On the other hand, Vassh et al. (2020) showed that the elements in this region could also be products of late-time fissioning of heavy nuclei, which would also deposit material in the lanthanide region. In that case, the abundances of these elements would be correlated with heavier *r*-process elements like Eu, instead of other light *r*-process elements like Zr. Indeed, Roederer et al. (2023) observed correlations of Ru, Rh, Pd, and Ag abundances of *r*-process stars with their [Eu/Fe] ratios, supporting this theory and providing an explanation for the observed dispersion in the abundances of these elements when scaled with Zr, as seen in Fig. 5. However, as shown by Roederer et al. (2023), Cd abundances of *r*-process stars do not show a similar correlation with [Eu/Fe]. We report here that this star adds to the evidence of a large dispersion in the Cd abundance, for which the cause continues to be unknown.

While the cause of such a dispersion of Cd abundances could be astrophysical, here we check for possible causes due to limitations in our stellar atmospheric models. For this purpose, we plot $\log\epsilon$(Cd), $\log\epsilon$(Cd/Zr), and $\log\epsilon$(Cd/Eu) abundances of all metal-poor stars with Cd abundance determined so far against their $T_{\rm eff}$, $\log g$, and [Fe/H] in Fig. 6. The stars included are HD 128 279 (Roederer et al. 2014b), HD 108 317 (Roederer et al. 2014b), HD 140 283 (Peterson, Barbuy & Spite 2020), HD 19 445 (Peterson, Barbuy & Spite 2020), HD 84 937 (Peterson, Barbuy & Spite 2020), BD $+17°3248$ (Roederer et al. 2022b), and HD 222 925 (Roederer et al. 2022a). We note that we only used Cd I abundances of these stars since these are typically the reported Cd abundances. We highlight the data points of J0051-1053 with a circular boundary around them.

We also fit the data with a linear least-square regression line, shown with golden-solid lines in Fig. 6. We list the Pearson correlation coefficient (*r*-value) and the corresponding *p*-value of the correlation in each panel. The *r*-value indicates the degree to which the two quantities are (anti)correlated with $(-1) + 1$ indicating the strongest (anti)correlation possible and 0 indicating no correlation. The *p*-value indicates the probability of a correlation equal to or stronger than what is observed, given the null hypothesis of no correlation. We find significant correlations ($-0.5 <$ *r*-value <0.5 and *p*-value <0.05) of $\log\epsilon$(Cd), $\log\epsilon$(Cd/Zr), and $\log\epsilon$(Cd/Eu) with respect to $T_{\rm eff}$, and of $\log\epsilon$(Cd/Zr) and $\log\epsilon$(Cd/Eu) with respect to $\log g$. We find no significant correlation of any Cd-based abundances with respect to [Fe/H].

Given the observed trends in the Cd abundance with respect to $T_{\rm eff}$ and $\log g$, we consider the case that the formation of the λ2288 Cd I line is strongly affected by NLTE. We note that Peterson, Barbuy & Spite (2020) used Cd II and Cd I lines for four metal-poor stars. While they derived consistent abundances between the two species, they commented that the consistent abundances were only possible by ignoring the HFS of the Cd II, as reported in Roederer & Lawler (2012). In the case that they used the HFS, inconsistent abundances were obtained. Such an inconsistency could further indicate strong NLTE effects for Cd I. With the present information, it is difficult to speculate the exact dependence of the NLTE effects on $T_{\rm eff}$ and $\log g$, if any, since their effects are degenerate. Therefore, we strongly urge the community to carry out detailed calculations to investigate the NLTE effects on Cd I abundances. We also encourage further theoretical investigations into a possible astrophysical origin for the dispersion in Cd abundances of metal-poor stars. Additional abundance determinations of Cd I and Cd II in metal-poor stars will also be helpful.

9.2.2 R-process pattern from the lanthanides to the third r-process peak

We find that, except for Ce and Eu, the *r*-process elements of J0051-1053 in the lanthanide region, from Ba ($Z = 56$) to Lu ($Z = 71$), adhere to the scaled *r*-process patterns of the SS and HD 222925. While the Ce abundance of J0051-1053 is higher than the scaled S.S *r*-process abundance by 0.24 dex, it agrees well with the scaled Ce abundance of HD 222925. Since we are using only two weak Ce II lines, we believe that a higher resolution and S/N study is warranted to better understand this discrepancy with the scaled SS Ce abundance.

On the other hand, the Eu abundance of J0051-1053 is lower than the the scaled Eu abundances of both the SS and HD 222 925 by

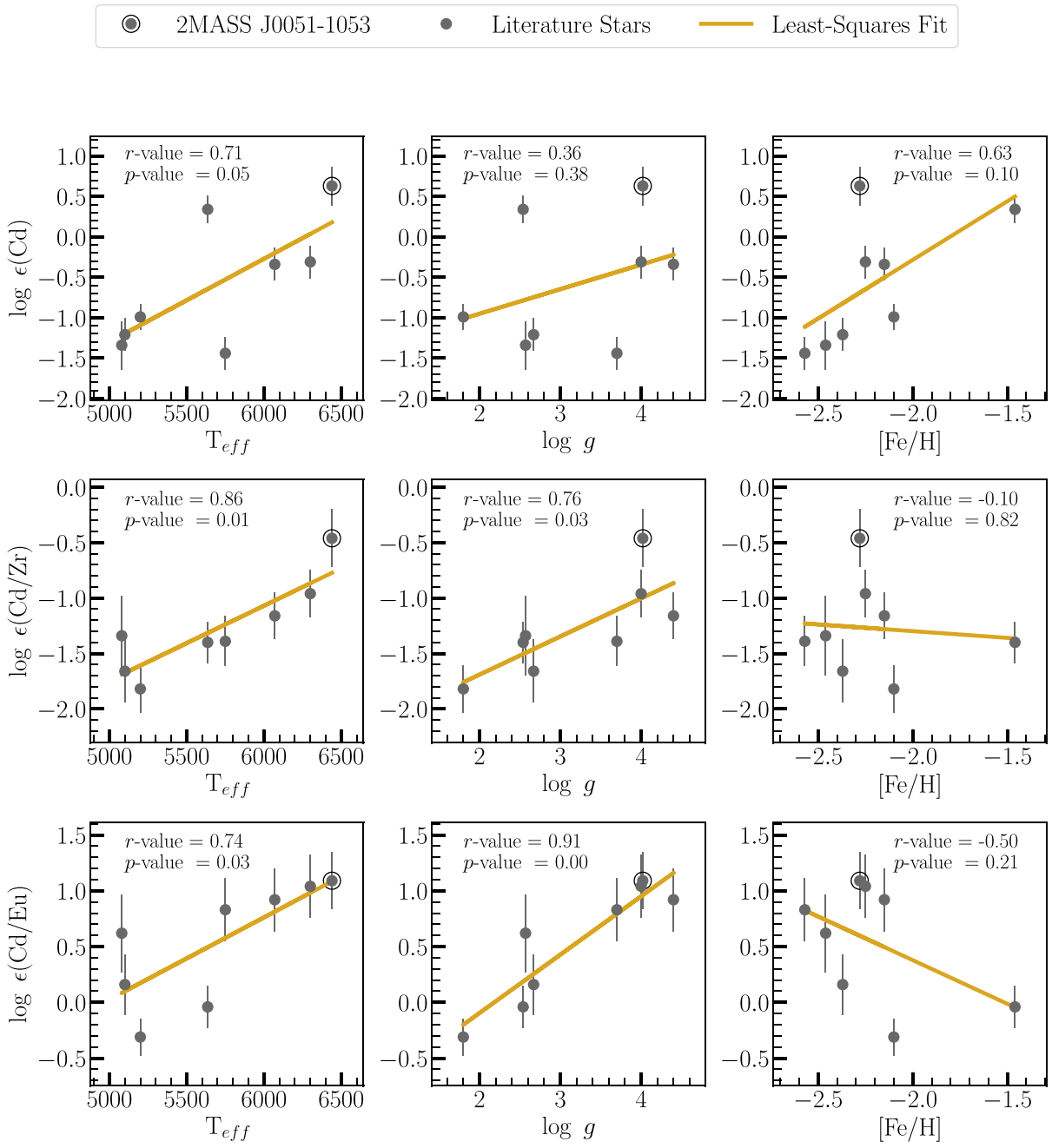

Figure 6. Cd abundances of J0051-1053 and other metal-poor stars (Roederer et al. 2022b, and references therein) with respect to stellar parameters of the stars, including $T_{\rm eff}$, log g, and [Fe/H]. The absolute Cd abundances are shown in the top row, Cd abundance scaled to Zr are shown in the middle row, and Cd abundance scaled to Eu are shown in the bottom row. Also shown is the least-square fit to the data with a golden-solid line. The Pearson correlation coefficient (r-value) and the corresponding probability of observing a correlation of at least this magnitude by chance (p-value) are listed in the top left corner for each panel.

$\sim$0.18 dex, which is more than 1σ. Since we have used five Eu II lines, all of which are of intermediate strength and have been well-established in the literature, we find this Eu discrepancy of note. Typically, discrepancies between the Eu abundance of RPE stars and the SS r-process pattern are not discovered or reported, since the SS r-process patterns are often scaled relative to the Eu abundance of the stars. However, as noted previously, in this study we have scaled the r-process pattern of the SS and HD 222 925 using the mean lanthanide abundance.

To understand this discrepancy, we consider the effects of NLTE on the formation of the Eu II lines. Zhao et al. (2016) estimated that for BD-04 3208, a dwarf metal-poor star with stellar parameters similar to J0051-1053 (Sitnova et al. 2015), the Eu NLTE abundance was 0.13 dex higher than the LTE abundance, when using the λ4129 Eu II line. A similar NLTE correction for the mean Eu abundance of J0051-1053, which is within 0.01 dex of the λ4129 abundance, would enable an agreement of its Eu abundance with the scaled Eu abundances of the SS and HD 222 295 within uncertainties.

While there have been several studies indicating that the universal *r*-process pattern extends to the third *r*-process peak (e.g. Cowan et al. 2005; Roederer et al. 2009, 2022a; Barbuy et al. 2011), there have been only five RPE stars with a Au abundance determined (Cowan et al. 2002; Sneden et al. 2003; Barbuy et al. 2011; Roederer et al. 2012a, 2022a). Similarly, there have been only ∼15 RPE stars with a Pt abundance determined (Cowan et al. 1996, 2002, 2005; Westin et al. 2000; Sneden et al. 2003; Barbuy et al. 2011; Roederer et al. 2012a, 2022a; Roederer & Lawler 2012). Therefore, the Au and Pt abundances of J0051-1053 are highly valuable. Indeed, we find that our results on the abundances of these elements, along with that of Os, uphold the case for the extension of the universal *r*-process pattern to the third *r*-process peak and to Au.

We also find that, with [Au/Fe] = +1.37, J0051-1053 has the highest enhancement in gold discovered in any star thus far. However, we note that this enhancement is not substantially different from what is found in other stars, which have +0.80 < [Au/Fe] <+1.28. Such enhancements in Au ([Au/Fe] > 0.0) remain at odds with the current Galactic chemical-enrichment models, which predict an under-production of [Au/Fe] levels by a factor of 5, or by 0.80 dex (Kobayashi, Karakas & Lugaro 2020). It is possible that such a discrepancy exists due to the observational bias of having Au abundance determined for only a few stars, which are also RPE. Therefore, there is an urgent need for more abundance determination of Au in metal-poor stars, which will require access to high-resolution space-based observations in the UV. To that end, this study serves as an important contribution.

10 CONCLUSIONS

We have performed a detailed chemical-abundance analysis of a very metal-poor ([Fe/H] = −2.31) turn-off RPE ([Eu/Fe] =1.37) star, 2MASS J00512646-1053170. For this, we obtained high-resolution HST/STIS and Magellan/MIKE spectroscopic data covering the UV (∼ 2275–3119 Å) and optical (3350–9500 Å) wavelengths. J0051-1053 may be the warmest highly RPE star studied in both the UV and optical domains thus far. As a result of the wide wavelength coverage, we determined abundances for 41 elements in total. We have identified several key chemical signatures that contribute to our understanding of the origin of these elements, especially the *r*-process elements, and motivate future theoretical and observational studies.

(i) We determined abundances for 16 light elements, including 26 individual species. We found that the light elements follow the typical trends of metal-poor stars (bottom panel of Fig. 3), indicating that their origin was primarily core-collapse supernovae.

(ii) We found that the most significant NLTE corrections are for Al I, K I, Cr I, and Mn I abundances. We show the LTE and NLTE-corrected abundances of individual species in the middle panel of Fig. 3.

(iii) We found that, even though the NLTE correction for Al I is large (+0.47 dex), it is still not sufficiently large to enable agreement with the LTE abundance of the dominant species, Al II, which remains ∼0.4 dex (∼2σ) higher than the NLTE-corrected Al I abundance. Based on this result, we urge the community to investigate the NLTE effects for Al I and Al II further.

(iv) Among the *r*-process elements, we determined detailed abundances for 23 elements and upper limits for six elements, ranging from the first *r*-process peak to the actinides (Fig. 4). We found that J0051-1053, like many other RPE stars, exhibits variations in its pattern of light *r*-process-elements. Specifically, Ge and Y are found to deviate from the lanthanide-scaled SS *r*-process pattern. However, we find that taking into account NLTE effects for the low-excitation Y II lines would enable a better agreement with the SS *r*-process pattern. On the other hand, Sr, Y, Zr, and Mo follow the benchmark light *r*-process-pattern of metal-poor stars identified by Roederer et al. (2022b; Fig. 5), adding evidence for a common source of light *r*-process elements in the early Universe.

(v) We found that [Ge/Fe] = +0.10 is significantly higher than observed in ∼20 metal-poor stars thus far, which exhibit [Ge/Fe] ∼−0.90 with a standard deviation of ∼0.28 dex. The similar [Ge/Fe] ratios observed in metal-poor stars has indicated a common origin for Ge and Fe in the early Universe, for instance α-rich freezeout. Therefore, the high [Ge/Fe] may indicate contribution from a production mechanism decoupled from that of Fe, such as the νp- or *r*-process.

(vi) Similarly, the Cd abundance observed for this star is the highest to date, adding to the dispersion observed in the Cd abundances of metal-poor stars, which still remains unexplained (Fig. 5). Here, we found that the log ϵ(Cd), log ϵ(Cd/Zr), and log ϵ(Cd/Eu) abundances of metal-poor stars are correlated to $T_{\rm eff}$ and log g of the stars, suggesting that the Cd I line may be severely affected by NLTE effects, causing the observed dispersion (Fig. 6). Therefore, we urge the community to theoretically study the NLTE effects for Cd I and Cd II, as well as revisit the astrophysical origin of this element.

(vii) We found that the lanthanides generally follow the universal *r*-process-pattern. However, the Eu abundance was found to be mildly discrepant from the universal pattern, which we found explainable by NLTE effects.

(viii) Additionally, the abundances of Os, Pt, and Au, uphold the case for the extension of the universal *r*-process-pattern to the third *r*-process peak (Fig. 4) – while this case has been suggested by previous studies, it remains to be firmly established due to the scarce number of abundances of elements like Pt and Au.

(ix) The abundance determination of Au marks J0051-1053 as only the sixth star with Au abundance determined. The enhancement in Au, relative to Fe, follows that of other metal-poor stars. These observed enhancements are five times higher than suggested by current Galactic chemical-evolution models, motivating the need for more abundance determinations of Au in metal-poor stars.

Overall, as part of the *R*-Process Alliance effort, this study adds to the sparse but growing number of RPE stars with extensive and detailed inventory of chemical abundances. We anticipate more such studies with UV and optical spectroscopy in the near future, especially as an increasing number of *r*-process-enhanced stars are identified (e.g. Hansen et al. 2018; Sakari et al. 2018; Ezzeddine et al. 2020; Holmbeck et al. 2020). However, as highlighted in this study, it will also be necessary to advance the theoretical NLTE studies, especially of *r*-process elements, in concurrence with the astrophysical studies, which critically depend on the reliable abundance determination of these elements.

ACKNOWLEDGEMENTS

This research is based on observations made with the NASA/ESA *Hubble Space Telescope* obtained from the Space Telescope Science Institute, which is operated by the Association of Universities for Research in Astronomy, Inc., under NASA contract NAS 5–26555. These observations are associated with program 15951. SPS acknowledges Jamie Tayar and Guilherme Limberg for helpful conversations. SPS and RE acknowledge support from NASA grant GO-15951 from the Space Telescope Science Institute, which is op-

erated by the Association of Universities for Research in Astronomy, Inc., under NASA contract NAS5–26555. RE acknowledges support from NSF grant AST-2206263. IUR acknowledges NSF grants AST 1815403 and AST 2205847, NASA Astrophysics Data Analysis Program grant 80NSSC21K0627, as well as NASA grants GO-15657, GO-15951, and AR-16630 from the Space Telescope Science Institute, which is operated by the Association of Universities for Research in Astronomy, Incorporated, under NASA contract NAS5-26555. TTH acknowledges support from the Swedish Research Council (VR 2021–05556). The work of VMP is supported by NOIRLab, which is managed by the Association of Universities for Research in Astronomy (AURA) under a cooperative agreement with the National Science Foundation. TCB acknowledges partial support from grant PHY 14–30152; Physics Frontier Center/JINA Center for the Evolution of the Elements (JINA-CEE), and from OISE-1927130: The International Research Network for Nuclear Astrophysics (IReNA), awarded by the US National Science Foundation. AF acknowledges support from NSF grant AST-1716251 and AST-2307436. APJ acknowledges support from NSF grant AST-2206264. CMS acknowledges support from the NSF grant AST 2206379.

DATA AVAILABILITY

The UV spectra of 2MASS J00512646-1053170 are publicly available on the *Mikulski Archive for Space Telescopes* and maybe obtained at doi:10.17909/cx55-zk52.

REFERENCES

Abohalima A., Frebel A., 2018, ApJS, 238, 36
Amarsi A. M., Asplund M., Collet R., Leenaarts J., 2016a, MNRAS, 455, 3735
Amarsi A. M., Lind K., Asplund M., Barklem P. S., Collet R., 2016b, MNRAS, 463, 1518
Arlandini C., Käppeler F., Wisshak K., Gallino R., Lugaro M., Busso M., Straniero O., 1999, ApJ, 525, 886
Asplund M., Grevesse N., Sauval A. J., Scott P., 2009, ARA&A, 47, 481
Bailer-Jones C. A. L., Rybizki J., Fouesneau M., Demleitner M., Andrae R., 2021, AJ, 161, 147
Barbuy B. et al., 2011, A&A, 534, A60
Beers T. C., Christlieb N., 2005, ARA&A, 43, 531
Beers T. C. et al., 2017, ApJ, 835, 81
Bergemann M., Cescutti G., 2010, A&A, 522, A9
Bergemann M., Pickering J. C., Gehren T., 2010, MNRAS, 401, 1334
Bergemann M., Kudritzki R.-P., Würl M., Plez B., Davies B., Gazak Z., 2013, ApJ, 764, 115
Bergemann M. et al., 2019, A&A, 631, A80
Bernstein R., Shectman S. A., Gunnels S. M., Mochnacki S., Athey A. E., 2003, in Iye M., Moorwood A. F. M.eds, Proc. SPIE Conf. Ser. Vol. 4841, Instrument Design and Performance for Optical/Infrared Ground-based Telescopes. SPIE, Bellingham. p. 1694,
Burbidge E. M., Burbidge G. R., Fowler W. A., Hoyle F., 1957, Rev. Mod. Phys., 29, 547
Cain M. et al., 2018, ApJ, 864, 43
Cameron A. G. W., 1957, PASP, 69, 201
Casagrande L., VandenBerg D. A., 2014, MNRAS, 444, 392
Casagrande L., Ramírez I., Meléndez J., Bessell M., Asplund M., 2010, A&A, 512, A54
Casey A. R., 2014, PhD thesis, Australian National University, Canberra
Castelli F., Kurucz R. L., 2003, in Piskunov N., Weiss W. W., Gray D. F.eds, Proceedings of the 210th Symposium of the International Astronomical Union Vol. 210, Modelling of Stellar Atmospheres. p. A20, preprint (arXiv:astro-ph/0405087)
Cayrel R., Kluwer Academic Publishers Dordrecht 1988, in Cayrel de Strobel G. , Spite M.eds, Proceedings of the 132nd Symposium of the International Astronomical Union Vol. 132, The Impact of Very High S/N Spectroscopy on Stellar Physics. p. 345
Cayrel R. et al., 2001, Nature, 409, 691
Cayrel R. et al., 2004, A&A, 416, 1117
Chiappini C., Frischknecht U., Meynet G., Hirschi R., Barbuy B., Pignatari M., Decressin T., Maeder A., 2011, Nature, 472, 454
Cowan J. J., Sneden C., Truran J. W., Burris D. L., 1996, ApJ, 460, L115
Cowan J. J. et al., 2002, ApJ, 572, 861
Cowan J. J. et al., 2005, ApJ, 627, 238
Cowan J. J., Sneden C., Roederer I. U., Lawler J. E., Hartog E. A. D., Sobeck J. S., Boesgaard A. M., 2020, ApJ, 890, 119
Cowan J. J., Sneden C., Lawler J. E., Aprahamian A., Wiescher M., Langanke K., Martínez-Pinedo G., Thielemann F.-K., 2021, Rev. Mod. Phys., 93, 15002
Curtis S., Ebinger K., Fröhlich C., Hempel M., Perego A., Liebendörfer M., Thielemann F.-K., 2019, ApJ, 870, 2
Curtis S., Miller J. M., Fröhlich C., Sprouse T., Lloyd-Ronning N., Mumpower M., 2023, ApJ, 945, L13
Cutri R. M. et al., 2003, VizieR Online Data Catalog, p. II/246
Delgado Mena E., Tsantaki M., Adibekyan V. Z., Sousa S. G., Santos N. C., González Hernández J. I., Israelian G., 2017, A&A, 606, A94
Den Hartog E. A., Herd M. T., Lawler J. E., Sneden C., Cowan J. J., Beers T. C., 2005, ApJ, 619, 639
Den Hartog E. A., Lawler J. E., Roederer I. U., 2020, ApJS, 248, 10
Den Hartog E. A., Lawler J. E., Roederer I. U., 2021, ApJS, 254, 5
Eichler M. et al., 2016, in Journal of Physics Conference Series. p. IOP Publishing Ltd, Lisbon, Portugal, 12054
Ezzeddine R., Frebel A., Plez B., 2017, ApJ, 847, 142
Ezzeddine R. et al., 2020, ApJ, 898, 150
Farouqi K., Kratz K. L., Pfeiffer B., Rauscher T., Thielemann F. K., Truran J. W., 2010, ApJ, 712, 1359
François P. et al., 2007, A&A, 476, 935
Frebel A., 2018, Annu. Rev. Nucl. Part. Sci., 68, 237
Frebel A. et al., 2006, ApJ, 652, 1585
Frebel A., Casey A. R., Jacobson H. R., Yu Q., 2013, ApJ, 769, 57
Fröhlich C., Martínez-Pinedo G., Liebendörfer M., Thielemann F. K., Bravo E., Hix W. R., Langanke K., Zinner N. T., 2006, Phys. Rev. Lett., 96, 142502
Goriely S., Arnould M., 2001, A&A, 379, 1113
Gull M., Frebel A., Hinojosa K., Roederer I. U., Ji A. P., Brauer K., 2021, ApJ, 912, 52
Hannaford P., Larkins P. L., Lowe R. M., 1981, J. Phys. B At. Mol. Phys., 14, 2321
Hansen C. J. et al., 2012, A&A, 545, A31
Hansen T. T. et al., 2018, ApJ, 858, 92
Hansen T. T. et al., 2019, Testing R-Process Nucleosynthesis Models With Two R-Process Enhanced Stars, HST Proposal. Cycle 27, ID. #15951
Hansen T. T. et al., 2021, ApJ, 915, 103
Henden A., Munari U., 2014, Contributions of the Astronomical Observatory Skalnaté Pleso, 43, 518
Hill V. et al., 2002, A&A, 387, 560
Hinkle K., Wallace L., Valenti J., Harmer D., 2000, Visible and Near Infrared Atlas of the Arcturus Spectrum 3727–9300 A , Astronomical Society of the Pacific Conference Series, San Francisco
Holmbeck E. M., Frebel A., McLaughlin G. C., Mumpower M. R., Sprouse T. M., Surman R., 2019, ApJ, 881, 5
Holmbeck E. M. et al., 2020, ApJS, 249, 30
Holmbeck E. M., Surman R., Roederer I. U., McLaughlin G. C., Frebel A., 2023, ApJ, 951, 30
Ivarsson S., Wahlgren G. M., Dai Z., Lundberg H., Leckrone D. S., 2004, A&A, 425, 353
Ji A. P., Frebel A., Simon J. D., Chiti A., 2016, ApJ, 830, 93
Ji A. P. et al., 2020, AJ, 160, 181
Ji A. P., Naidu R. P., Brauer K., Ting Y.-S., Simon J. D., 2023, MNRAS, 513, 3, 4467
Keeping E., 1962, Introduction to Statistical Inference. Van Nostrand-Reinhold, Princeton, NJ
Kelson D. D., 2003, PASP, 115, 688

Kelson D. D., Illingworth G. D., van Dokkum P. G., Franx M., 2000, ApJ, 531, 159
Kimble R. A. et al., 1998, ApJ, 492, L83
Kobayashi C., Karakas A. I., Lugaro M., 2020, ApJ, 900, 179
Koppelman H. H., Helmi A., Massari D., Roelenga S., Bastian U., 2019, A&A, 625, A5
Kowkabany J. et al., 2022, preprint (arXiv:2209.02184)
Kramida A., Ralchenko Yu., Reader J., NIST ASD Team, 2022, NIST Atomic Spectra Database (ver. 5.10), [Online]. Available: https://physics.nist.gov/asd [2016, January 31]. National Institute of Standards and Technology, Gaithersburg, MD.
Limberg G. et al., 2021, ApJ, 913, L28
Lind K., Melendez J., Asplund M., Collet R., Magic Z., 2013, A&A, 554, A96
Lind K. et al., 2022, A&A, 665, A33
Lippuner J., Fernández R., Roberts L. F., Foucart F., Kasen D., Metzger B. D., Ott C. D., 2017, MNRAS, 472, 904
McCall M. L., 2004, AJ, 128, 2144
Marshall J. L. et al., 2019, ApJ, 882, 177
Mashonkina L. I., Belyaev A. K., Shi J. R., 2016, Astron. Lett., 42, 366
Mashonkina L., Sitnova T., Belyaev A. K., 2017, A&A, 605, A53
Masseron T. et al., 2014, A&A, 571, A47
Montes F. et al., 2007, ApJ, 671, 1685
National Academies of Sciences E., Medicine, 2021, Pathways to Discovery in Astronomy and Astrophysics for the 2020s, The National Academies Press. Washington, DC.
Nordlander T., Lind K., 2017, A&A, 607, A75
Norris J. E., Yong D., Frebel A., Ryan S. G., 2023, MNRAS, 522, 1358
Peterson R. C., 2011, ApJ, 742, 21
Peterson R. C., Barbuy B., Spite M., 2020, A&A, 638, A64
Placco V. M., Frebel A., Beers T. C., Stancliffe R. J., 2014, ApJ, 797, 21
Placco V. M. et al., 2015, ApJ, 812, 109
Placco V. M. et al., 2020, ApJ, 897, 78
Placco V. M., Sneden C., Roederer I. U., Lawler J. E., Den Hartog E. A., Hejazi N., Maas Z., Bernath P., 2021a. linemake: Line list generator, Astrophysics Source Code Library, record ascl:2104.027
Placco V. M., Sneden C., Roederer I. U., Lawler J. E., Den Hartog E. A., Hejazi N., Maas Z., Bernath P., 2021b, Res. Notes Am. Astron. Soc., 5, 92
Plez B. et al., 2004, A&A, 428, L9
Prantzos N., 2012, A&A, 542, A67
Prantzos N., Abia C., Cristallo S., Limongi M., Chieffi A., 2020, MNRAS, 491, 1832
Quinet P., Palmeri P., Biémont É., Jorissen A., van Eck S., Svanberg S., Xu H. L., Plez B., 2006, A&A, 448, 1207
Roederer I. U., Barklem P. S., 2018, ApJ, 857, 2
Roederer I. U., Lawler J. E., 2012, ApJ, 750, 76
Roederer I. U., Lawler J. E., 2021, ApJ, 912, 119
Roederer I. U., Kratz K.-L., Frebel A., Christlieb N., Pfeiffer B., Cowan J. J., Sneden C., 2009, ApJ, 698, 1963
Roederer I. U., Sneden C., Thompson I. B., Preston G. W., Shectman S. A., 2010a, ApJ, 711, 573
Roederer I. U., Sneden C., Lawler J. E., Cowan J. J., 2010b, ApJ, 714, L123
Roederer I. U. et al., 2012a, ApJS, 203, 27
Roederer I. U., Lawlor James, 2012, ApJ, 750, 76,
Roederer I. U., Preston G. W., Thompson I. B., Shectman S. A., Sneden C., Burley G. S., Kelson D. D., 2014a, AJ, 147, 136
Roederer I. U. et al., 2014b, ApJ, 791, 32
Roederer I. U., Placco V. M., Beers T. C., 2016, ApJ, 824, L19
Roederer I. U., Sakari C. M., Placco V. M., Beers T. C., Ezzeddine R., Frebel A., Hansen T. T., 2018, ApJ, 865, 129
Roederer I. U. et al., 2022a, ApJS, 260, 27
Roederer I. U. et al., 2022b, ApJ, 936, 84
Roederer I. U. et al., 2023, Science, 382, 1177
Sakari C. M. et al., 2018, ApJ, 868, 110
Schatz H., Toenjes R., Pfeiffer B., Beers T. C., Cowan J. J., Hill V., Kratz K.-L., 2002, ApJ, 579, 626
Schlafly E. F., Finkbeiner D. P., 2011, ApJ, 737, 103
Shah S. P. et al., 2023, ApJ, 948, 122
Siegel D. M., Barnes J., Metzger B. D., 2019, Nature, 569, 241
Siqueira Mello C. et al., 2013, A&A, 550, A122
Siqueira Mello C. et al., 2014, A&A, 565, A93
Sitnova T. et al., 2015, ApJ, 808, 148
Sitnova T. M., Yakovleva S. A., Belyaev A. K., Mashonkina L. I., 2020, Astron. Lett., 46, 120
Sitnova T. M., Yakovleva S. A., Belyaev A. K., Mashonkina L. I., 2022, MNRAS, 515, 1510
Sneden C. A., 1973, PhD thesis, University of Texas, Austin
Sneden C., Cowan J. J., Burris D. L., Truran J. W., 1998, ApJ, 496, 235
Sneden C., Cowan J. J., Ivans I. I., Fuller G. M., Burles S., Beers T. C., Lawler J. E., 2000, ApJ, 533, L139
Sneden C. et al., 2003, ApJ, 591, 936
Sneden C., Cowan J. J., Gallino R., 2008, ARA&A, 46, 241
Sneden C., Lawler J. E., Cowan J. J., Ivans I. I., Den Hartog E. A., 2009, ApJS, 182, 80
Sneden C., Boesgaard A. M., Cowan J. J., Roederer I. U., Den Hartog E. A., Lawler J. E., 2023, The Astrophysical Journal. 953, 18
Sobeck J. S. et al., 2011, AJ, 141, 175
Spite F., Spite M., 1982, A&A, 115, 357
Storm N., Bergemann M., 2023, MNRAS, 525, 3718
Takeda Y., Zhao G., Chen Y.-Q., Qiu H.-M., Takada-Hidai M., 2002, PASJ, 54, 275
Thévenin F., Idiart T. P., 1999, ApJ, 521, 753
Vassh N. et al., 2019, J. Phys. G Nucl. Phys., 46, 65202
Vassh N., Mumpower M. R., McLaughlin G. C., Sprouse T. M., Surman R., 2020, ApJ, 896, 28
Venn K. A., Irwin M., Shetrone M. D., Tout C. A., Hill V., Tolstoy E., 2004, AJ, 128, 1177
Wanajo S., 2013, ApJ, 770, L22
Wang E. X., Nordlander T., Asplund M., Amarsi A. M., Lind K., Zhou Y., 2021, MNRAS, 500, 2159
Westin J., Sneden C., Gustafsson B., Cowan J. J., 2000, ApJ, 530, 783
Woodgate B. E. et al., 1998, PASP, 110, 1183
Zhang M., Zhou L., Gao Y., Yu Q., Wang X., Wang Q., Gong Y., Dai Z., 2018, J. Phys. B At. Mol. Phys., 51, 205001
Zhao G. et al., 2016, ApJ, 833, 225

APPENDIX A: LINELIST

Table A1. Wavelength, excitation potential, and oscillator strength of all absorption lines used are listed. Also listed is the abundance determination technique used i.e. spectral synthesis (syn) or EW measurement (ew). In the final columns, the abundance of the line and the associated systematic uncertainty are listed.

Species	Wavelength (Å)	χ (eV)	log gf	Type	log ϵ(X)	σ_{sys}
Li I	6707.8	0.0	0.17	syn	2.37	0.05
O I	7771.94	9.15	0.37	syn	7.12	0.05
O I	7774.17	9.15	0.22	syn	7.09	0.05
O I	7775.39	9.15	0.00	syn	7.04	0.05
Na I	5889.95	0.0	0.11	eqw	4.03	0.09
Na I	5895.92	0.0	− 0.19	eqw	3.92	0.07
Na I	8183.26	2.1	0.24	eqw	3.93	0.03
Na I	8194.81	2.1	0.54	eqw	4.07	0.03
Mg I	2736.54	2.72	− 1.01	syn	5.64	0.05
Mg I	2936.74	2.71	− 2.27	syn	5.68	0.06
Mg I	4057.51	4.35	− 0.90	syn	5.85	0.02
Mg I	4167.27	4.35	− 0.74	syn	5.88	0.02
Mg I	4571.1	0.0	− 5.62	syn	5.72	0.07
Mg I	4702.99	4.35	− 0.44	syn	5.75	0.03
Mg I	5172.68	2.71	− 0.36	syn	5.64	0.08
Mg I	5183.60	2.72	− 0.17	syn	5.63	0.09
Mg I	5528.4	4.35	− 0.55	syn	5.65	0.03
Mg II	2928.63	4.42	− 0.53	syn	5.7	0.08
Al I	3943.0	0.0	− 0.64	syn	3.42	0.07
Al I	3961.52	0.01	− 0.33	syn	3.23	0.06
Al II	2669.16	0.0	− 4.98	syn	4.18	0.06
Si I	2987.64	0.78	− 1.97	syn	5.58	0.08
Si I	3905.52	1.91	− 1.04	syn	5.53	0.1
Si II	2334.41	0.0	− 5.09	syn	5.59	0.05
Si II	2350.17	0.04	− 5.12	syn	5.6	0.07
Si II	6371.36	8.12	− 0.08	syn	5.47	0.04
S I	6757.13	7.87	− 0.13	syn	<5.98	–
K I	7698.96	0.0	− 0.18	eqw	3.33	0.05
Ca I	4226.74	0.0	0.24	eqw	4.36	0.11
Ca I	4283.01	1.89	− 0.2	eqw	4.4	0.05
Ca I	4318.65	1.9	− 0.21	eqw	4.34	0.05
Ca I	4425.44	1.88	− 0.41	eqw	4.49	0.05
Ca I	4434.96	1.89	− 0.06	eqw	4.43	0.05
Ca I	4435.69	1.89	− 0.55	eqw	4.56	0.04
Ca I	4454.78	1.9	0.26	eqw	4.35	0.05
Ca I	4455.89	1.9	− 0.55	eqw	4.46	0.05
Ca I	4578.55	2.52	− 0.67	eqw	4.58	0.04
Ca I	5261.71	2.52	− 0.6	eqw	4.61	0.04
Ca I	5512.98	2.93	− 0.45	eqw	4.59	0.03
Ca I	5581.97	2.52	− 0.58	eqw	4.49	0.04
Ca I	5588.76	2.52	0.3	eqw	4.43	0.04
Ca I	5590.12	2.52	− 0.6	eqw	4.58	0.04
Ca I	5857.45	2.93	0.17	eqw	4.5	0.03
Ca I	6102.72	1.88	− 0.81	eqw	4.39	0.05
Ca I	6122.22	1.89	− 0.33	eqw	4.46	0.05
Ca I	6162.17	1.9	− 0.11	eqw	4.46	0.05
Ca I	6169.06	2.52	− 0.87	eqw	4.62	0.04
Ca I	6169.56	2.53	− 0.6	eqw	4.6	0.04
Ca I	6439.07	2.52	0.33	eqw	4.45	0.04
Ca I	6449.81	2.52	− 0.55	eqw	4.52	0.04
Ca I	6499.65	2.52	− 0.81	eqw	4.31	0.04
Ca I	6717.69	2.71	− 0.58	eqw	4.46	0.04
Sc II	2551.0	–	–	syn	1.13	0.04
Sc II	3572.53	0.02	0.27	syn	1.17	0.09
Sc II	3576.34	0.01	0.01	syn	1.13	0.09
Sc II	3590.47	0.02	− 0.55	syn	1.1	0.04
Sc II	3630.74	0.01	0.22	syn	0.99	0.05
Sc II	4246.81	0.32	0.24	syn	1.15	0.05
Sc II	4314.08	0.62	− 0.1	syn	1.14	0.02
Sc II	4320.73	0.6	− 0.25	syn	1.1	0.04
Sc II	4324.98	0.59	− 0.44	syn	1.02	0.04
Sc II	4374.45	0.62	− 0.42	syn	1.12	0.03
Sc II	4400.38	0.6	− 0.54	syn	1.09	0.04
Sc II	4415.54	0.59	− 0.67	syn	1.03	0.04
Sc II	4670.4	1.36	− 0.58	syn	1.15	0.04
Ti I	3989.76	0.02	− 0.13	eqw	3.18	0.07
Ti I	3998.64	0.05	0.02	eqw	3.13	0.07
Ti I	4512.73	0.84	− 0.4	eqw	3.29	0.06
Ti I	4518.02	0.83	− 0.25	eqw	3.19	0.06
Ti I	4533.24	0.85	0.54	eqw	3.1	0.06
Ti I	4534.78	0.84	0.35	eqw	3.1	0.06
Ti I	4681.91	0.05	− 1.01	eqw	3.38	0.07
Ti I	4981.73	0.84	0.57	eqw	3.05	0.06
Ti I	4991.07	0.84	0.45	eqw	3.13	0.06
Ti I	4999.5	0.83	0.32	eqw	3.22	0.06
Ti I	5173.74	0.0	− 1.06	eqw	3.36	0.07
Ti I	5192.97	0.02	− 0.95	eqw	3.31	0.07
Ti II	2761.29	1.08	− 1.35	syn	3.0	0.07
Ti II	2841.93	0.61	− 0.59	syn	3.18	0.09
Ti II	3029.73	1.57	− 0.35	syn	3.04	0.04
Ti II	3048.76	1.58	− 1.18	syn	3.2	0.07
Ti II	3340.34	0.11	− 0.53	eqw	3.26	0.18
Ti II	3343.76	0.15	− 1.18	eqw	3.03	0.11
Ti II	3372.79	0.01	0.28	eqw	3.48	0.14
Ti II	3387.83	0.03	− 0.41	eqw	3.46	0.19
Ti II	3456.38	2.06	− 0.11	eqw	2.65	0.04
Ti II	3477.18	0.12	− 0.95	eqw	3.36	0.17
Ti II	3489.74	0.14	− 2.0	eqw	3.21	0.07
Ti II	3491.05	0.11	− 1.1	eqw	3.22	0.14
Ti II	3759.29	0.61	0.28	eqw	3.13	0.17
Ti II	3761.32	0.57	0.18	eqw	3.06	0.17
Ti II	3913.46	1.12	− 0.36	eqw	3.03	0.09
Ti II	4028.34	1.89	− 0.92	eqw	3.08	0.03
Ti II	4394.06	1.22	− 1.77	eqw	3.1	0.04
Ti II	4395.03	1.08	− 0.54	eqw	3.13	0.09
Ti II	4395.84	1.24	− 1.93	eqw	3.09	0.04
Ti II	4399.77	1.24	− 1.2	eqw	3.06	0.04
Ti II	4417.71	1.17	− 1.19	eqw	3.06	0.04
Ti II	4418.33	1.24	− 1.99	eqw	3.17	0.04
Ti II	4443.8	1.08	− 0.71	eqw	3.09	0.07
Ti II	4444.55	1.12	− 2.2	eqw	3.04	0.04
Ti II	4450.48	1.08	− 1.52	eqw	3.1	0.04
Ti II	4464.45	1.16	− 1.81	eqw	3.08	0.04
Ti II	4470.85	1.17	− 2.02	eqw	2.89	0.04
Ti II	4501.27	1.12	− 0.77	eqw	3.12	0.07
Ti II	4533.96	1.24	− 0.53	eqw	3.06	0.07
Ti II	4571.97	1.57	− 0.31	eqw	3.07	0.06
Ti II	4657.2	1.24	− 2.29	eqw	3.08	0.04
Ti II	4708.66	1.24	− 2.35	eqw	3.16	0.04
Ti II	4798.53	1.08	− 2.66	eqw	3.17	0.04
Ti II	5188.69	1.58	− 1.05	eqw	3.12	0.04
Ti II	5226.54	1.57	− 1.26	eqw	3.07	0.04
Ti II	5336.79	1.58	− 1.6	eqw	3.01	0.04
Ti II	5381.02	1.57	− 1.97	eqw	3.16	0.04
Ti II	5418.77	1.58	− 2.13	eqw	3.32	0.04
V I	4111.78	0.3	0.4	syn	2.05	0.1
V II	2679.32	0.03	− 0.63	syn	1.96	0.05
V II	2688.71	0.04	− 0.98	syn	2.02	0.09
V II	2700.93	0.04	− 0.37	syn	2.05	0.05

Table A1 – *continued*

Species	Wavelength (Å)	χ (eV)	log *gf*	Type	log ϵ(X)	σ_{sys}
V II	2707.86	0.0	− 1.39	syn	2.11	0.13
V II	2880.03	0.35	− 0.64	syn	1.9	0.1
V II	2903.07	0.32	− 0.7	syn	1.89	0.05
V II	3517.3	1.13	− 0.24	syn	1.89	0.03
V II	3545.2	1.09	− 0.32	syn	2.05	0.02
V II	3715.46	1.57	− 0.22	syn	2.0	0.04
V II	3727.34	1.69	− 0.23	syn	1.95	0.04
V II	3903.25	1.48	− 0.91	syn	1.98	0.08
V II	4005.7	1.82	− 0.45	syn	1.92	0.04
V II	4023.38	1.8	− 0.61	syn	2.03	0.03
Cr I	3015.2	0.96	− 0.2	syn	3.23	0.07
Cr I	3021.56	1.03	0.61	syn	3.2	0.2
Cr I	3908.76	1.0	− 1.05	syn	3.42	0.06
Cr I	4616.12	0.98	− 1.19	syn	3.4	0.02
Cr I	4646.16	1.03	− 0.74	syn	3.3	0.05
Cr I	4652.16	1.0	− 1.04	syn	3.31	0.04
Cr I	5206.04	0.94	0.02	syn	3.29	0.08
Cr I	5345.8	1.0	− 0.95	syn	3.3	0.06
Cr II	2666.01	1.51	− 0.08	syn	3.44	0.05
Cr II	2668.71	1.49	− 0.55	syn	3.42	0.0
Cr II	2671.81	1.51	− 0.38	syn	3.51	0.08
Cr II	2677.16	1.55	0.35	syn	3.51	0.07
Cr II	2687.09	1.51	− 0.62	syn	3.5	0.02
Cr II	2751.87	1.53	− 0.29	syn	3.51	0.2
Cr II	2856.76	2.43	− 0.59	syn	3.44	0.12
Cr II	2865.33	2.42	− 0.71	syn	3.52	0.06
Cr II	2867.09	2.43	− 0.5	syn	3.42	0.07
Cr II	2876.24	1.51	− 0.87	syn	3.39	0.05
Cr II	2878.45	1.55	− 1.27	syn	3.38	0.07
Cr II	3408.77	2.48	− 0.27	syn	3.3	0.07
Cr II	4588.2	4.07	− 0.65	syn	3.31	0.02
Cr II	4618.81	4.07	− 0.89	syn	3.33	0.03
Mn I	2298.84	2.89	− 1.75	syn	3.12	0.01
Mn I	2610.51	3.07	− 0.28	syn	2.8	0.11
Mn I	2706.14	2.95	− 1.34	syn	2.75	0.06
Mn I	4041.35	2.11	0.28	syn	2.78	0.03
Mn I	4055.54	2.14	− 0.08	syn	2.82	0.11
Mn I	4754.04	2.28	− 0.08	syn	2.8	0.06
Mn I	4762.37	2.89	0.3	syn	2.83	0.04
Mn I	4783.43	2.3	0.04	syn	2.83	0.04
Mn II	2939.31	1.17	0.11	syn	3.05	0.03
Mn II	2949.20	1.18	0.25	syn	2.89	0.06
Mn II	3441.99	1.78	− 0.35	syn	2.87	0.03
Mn II	3460.32	1.81	− 0.63	syn	2.87	0.07
Mn II	3482.90	1.83	− 0.84	syn	2.97	0.07
Mn II	3488.68	1.85	− 0.94	syn	2.82	0.05
Fe I	2283.66	0.11	− 2.22	syn	5.23	0.1
Fe I	2294.41	0.11	− 1.54	syn	5.25	0.04
Fe I	2485.99	0.92	− 1.61	syn	5.14	0.1
Fe I	2539.36	0.92	− 1.79	syn	5.2	0.1
Fe I	2636.48	0.92	− 2.04	syn	5.3	0.08
Fe I	2641.64	0.92	− 1.32	syn	4.95	0.05
Fe I	2644.0	1.01	− 0.91	syn	4.94	0.05
Fe I	2645.42	0.11	− 2.75	syn	5.02	0.05
Fe I	2647.56	0.05	− 2.42	syn	5.25	0.07
Fe I	2666.4	0.96	− 1.87	syn	5.2	0.07
Fe I	2680.45	0.99	− 1.74	syn	4.95	0.05
Fe I	2690.07	0.0	− 2.72	syn	5.12	0.04
Fe I	2728.02	0.92	− 1.46	syn	5.16	0.09
Fe I	2730.98	1.01	− 1.73	syn	5.18	0.11
Fe I	2838.12	0.99	− 1.11	syn	5.18	0.06
Fe I	2877.3	1.48	− 1.3	syn	5.16	0.03
Fe I	2960.66	2.95	− 1.0	syn	5.2	0.09
Fe I	2966.9	0.0	− 0.4	syn	5.31	0.11
Fe I	3009.57	0.92	− 0.76	syn	5.25	0.1

Table A1 – *continued*

Species	Wavelength (Å)	χ (eV)	log *gf*	Type	log ϵ(X)	σ_{sys}
Fe I	3024.03	0.11	− 1.48	syn	5.23	0.16
Fe I	3059.09	0.05	− 0.69	syn	5.1	0.06
Fe I	3406.8	2.22	− 0.96	eqw	5.21	0.08
Fe I	3440.61	0.0	− 0.67	eqw	5.27	0.19
Fe I	3440.99	0.05	− 0.96	eqw	5.43	0.2
Fe I	3451.91	2.22	− 1.0	eqw	5.17	0.07
Fe I	3490.57	0.05	− 1.1	eqw	5.36	0.2
Fe I	3540.12	2.87	− 0.71	eqw	5.14	0.07
Fe I	3565.38	0.96	− 0.13	eqw	5.38	0.18
Fe I	3608.86	1.01	− 0.09	eqw	5.35	0.18
Fe I	3618.77	0.99	− 0.0	eqw	5.22	0.18
Fe I	3647.84	0.92	− 0.14	eqw	4.93	0.16
Fe I	3727.62	0.96	− 0.61	eqw	5.08	0.15
Fe I	3742.62	2.94	− 0.81	eqw	5.06	0.05
Fe I	3758.23	0.96	− 0.01	eqw	5.05	0.15
Fe I	3786.68	1.01	− 2.18	eqw	5.18	0.07
Fe I	3787.88	1.01	− 0.84	eqw	5.12	0.13
Fe I	3815.84	1.48	0.24	eqw	5.08	0.15
Fe I	3849.97	1.01	− 0.86	eqw	5.21	0.14
Fe I	3856.37	0.05	− 1.28	eqw	5.27	0.18
Fe I	3865.52	1.01	− 0.95	eqw	5.17	0.13
Fe I	3878.02	0.96	− 0.9	eqw	5.22	0.14
Fe I	3899.71	0.09	− 1.52	eqw	5.25	0.16
Fe I	3902.95	1.56	− 0.44	eqw	5.07	0.12
Fe I	3920.26	0.12	− 1.73	eqw	5.32	0.15
Fe I	3922.91	0.05	− 1.63	eqw	5.35	0.17
Fe I	3949.95	2.18	− 1.25	eqw	5.22	0.06
Fe I	3977.74	2.2	− 1.12	eqw	5.12	0.06
Fe I	4005.24	1.56	− 0.58	eqw	5.12	0.11
Fe I	4045.81	1.49	0.28	eqw	5.18	0.14
Fe I	4058.22	3.21	− 1.18	eqw	5.39	0.05
Fe I	4063.59	1.56	0.06	eqw	5.21	0.15
Fe I	4067.98	3.21	− 0.53	eqw	5.28	0.05
Fe I	4070.77	3.24	− 0.87	eqw	5.36	0.05
Fe I	4071.74	1.61	− 0.01	eqw	5.16	0.14
Fe I	4114.44	2.83	− 1.3	eqw	4.97	0.05
Fe I	4132.06	1.61	− 0.68	eqw	5.26	0.11
Fe I	4134.68	2.83	− 0.65	eqw	5.21	0.05
Fe I	4143.87	1.56	− 0.51	eqw	5.16	0.12
Fe I	4147.67	1.49	− 2.07	eqw	5.26	0.07
Fe I	4154.5	2.83	− 0.69	eqw	5.13	0.05
Fe I	4156.8	2.83	− 0.81	eqw	5.21	0.05
Fe I	4157.78	3.42	− 0.4	eqw	5.14	0.05
Fe I	4174.91	0.91	− 2.94	eqw	5.17	0.07
Fe I	4175.64	2.85	− 0.83	eqw	5.28	0.05
Fe I	4181.76	2.83	− 0.37	eqw	5.19	0.06
Fe I	4182.38	3.02	− 1.18	eqw	5.08	0.05
Fe I	4184.89	2.83	− 0.87	eqw	5.14	0.05
Fe I	4187.04	2.45	− 0.56	eqw	5.15	0.06
Fe I	4187.8	2.42	− 0.51	eqw	5.14	0.06
Fe I	4191.43	2.47	− 0.67	eqw	5.17	0.06
Fe I	4195.33	3.33	− 0.49	eqw	5.21	0.05
Fe I	4199.1	3.05	0.16	eqw	5.07	0.06
Fe I	4202.03	1.49	− 0.69	eqw	5.18	0.11
Fe I	4216.18	0.0	− 3.36	eqw	5.36	0.09
Fe I	4217.55	3.43	− 0.48	eqw	5.22	0.05
Fe I	4222.21	2.45	− 0.91	eqw	5.09	0.06
Fe I	4227.43	3.33	0.27	eqw	5.19	0.05
Fe I	4233.6	2.48	− 0.6	eqw	5.17	0.06
Fe I	4238.81	3.4	− 0.23	eqw	5.2	0.05
Fe I	4250.12	2.47	− 0.38	eqw	5.14	0.06
Fe I	4250.79	1.56	− 0.71	eqw	5.19	0.1
Fe I	4260.47	2.4	0.08	eqw	5.11	0.09
Fe I	4271.15	2.45	− 0.34	eqw	5.13	0.07

Table A1 – *continued*

Species	Wavelength (Å)	χ (eV)	log gf	Type	log ϵ(X)	σ_{sys}
Fe I	4271.76	1.49	− 0.17	eqw	5.22	0.15
Fe I	4282.4	2.18	− 0.78	eqw	5.12	0.06
Fe I	4325.76	1.61	0.01	eqw	5.11	0.14
Fe I	4352.73	2.22	− 1.29	eqw	5.22	0.06
Fe I	4375.93	0.0	− 3.0	eqw	5.23	0.09
Fe I	4388.41	3.6	− 0.68	eqw	5.21	0.04
Fe I	4404.75	1.56	− 0.15	eqw	5.21	0.14
Fe I	4415.12	1.61	− 0.62	eqw	5.19	0.11
Fe I	4427.31	0.05	− 2.92	eqw	5.25	0.09
Fe I	4430.61	2.22	− 1.73	eqw	5.16	0.06
Fe I	4442.34	2.2	− 1.23	eqw	5.24	0.06
Fe I	4443.19	2.86	− 1.04	eqw	5.08	0.05
Fe I	4447.72	2.22	− 1.36	eqw	5.23	0.06
Fe I	4461.65	0.09	− 3.19	eqw	5.28	0.08
Fe I	4466.55	2.83	− 0.6	eqw	5.15	0.05
Fe I	4484.22	3.6	− 0.64	eqw	5.04	0.04
Fe I	4494.56	2.2	− 1.14	eqw	5.21	0.06
Fe I	4531.15	1.48	− 2.1	eqw	5.19	0.07
Fe I	4592.65	1.56	− 2.46	eqw	5.36	0.07
Fe I	4602.94	1.49	− 2.21	eqw	5.28	0.07
Fe I	4619.29	3.6	− 1.06	eqw	5.07	0.04
Fe I	4637.5	3.28	− 1.29	eqw	5.12	0.05
Fe I	4647.43	2.95	− 1.35	eqw	5.21	0.05
Fe I	4668.13	3.27	− 1.08	eqw	5.17	0.05
Fe I	4733.59	1.49	− 2.99	eqw	5.37	0.07
Fe I	4736.77	3.21	− 0.67	eqw	5.14	0.05
Fe I	4871.32	2.87	− 0.34	eqw	5.07	0.05
Fe I	4872.14	2.88	− 0.57	eqw	5.05	0.05
Fe I	4890.76	2.88	− 0.38	eqw	5.12	0.05
Fe I	4891.49	2.85	− 0.11	eqw	5.11	0.06
Fe I	4903.31	2.88	− 0.89	eqw	5.11	0.05
Fe I	4918.99	2.86	− 0.34	eqw	5.14	0.06
Fe I	4920.5	2.83	0.07	eqw	5.11	0.07
Fe I	4938.81	2.88	− 1.08	eqw	5.17	0.05
Fe I	4939.69	0.86	− 3.25	eqw	5.29	0.07
Fe I	4946.39	3.37	− 1.11	eqw	5.09	0.05
Fe I	4966.09	3.33	− 0.79	eqw	5.18	0.05
Fe I	5001.86	3.88	− 0.01	eqw	5.29	0.04
Fe I	5006.12	2.83	− 0.62	eqw	5.1	0.05
Fe I	5014.94	3.94	− 0.18	eqw	5.22	0.04
Fe I	5049.82	2.28	− 1.36	eqw	5.25	0.06
Fe I	5051.63	0.92	− 2.76	eqw	5.33	0.07
Fe I	5068.77	2.94	− 1.04	eqw	5.15	0.05
Fe I	5079.74	0.99	− 3.24	eqw	5.32	0.07
Fe I	5083.34	0.96	− 2.84	eqw	5.13	0.07
Fe I	5123.72	1.01	− 3.06	eqw	5.39	0.07
Fe I	5127.36	0.92	− 3.25	eqw	5.29	0.07
Fe I	5133.69	4.18	0.36	eqw	5.13	0.04
Fe I	5150.84	0.99	− 3.04	eqw	5.23	0.07
Fe I	5171.6	1.49	− 1.72	eqw	5.23	0.07
Fe I	5191.45	3.04	− 0.55	eqw	5.19	0.05
Fe I	5192.34	3.0	− 0.42	eqw	5.18	0.05
Fe I	5194.94	1.56	− 2.02	eqw	5.18	0.07
Fe I	5215.18	3.27	− 0.86	eqw	5.06	0.05
Fe I	5216.27	1.61	− 2.08	eqw	5.24	0.07
Fe I	5232.94	2.94	− 0.06	eqw	5.08	0.06
Fe I	5266.56	3.0	− 0.38	eqw	5.15	0.05
Fe I	5281.79	3.04	− 0.83	eqw	5.01	0.05
Fe I	5283.62	3.24	− 0.45	eqw	5.18	0.05
Fe I	5324.18	3.21	− 0.11	eqw	5.11	0.05
Fe I	5339.93	3.27	− 0.63	eqw	4.95	0.05
Fe I	5341.02	1.61	− 1.95	eqw	5.33	0.07
Fe I	5364.87	4.45	0.23	eqw	5.16	0.04

Table A1 – *continued*

Species	Wavelength (Å)	χ (eV)	log gf	Type	log ϵ(X)	σ_{sys}
Fe I	5367.47	4.42	0.44	eqw	5.06	0.04
Fe I	5369.96	4.37	0.54	eqw	5.03	0.04
Fe I	5371.49	0.96	− 1.64	eqw	5.3	0.1
Fe I	5383.37	4.31	0.64	eqw	5.1	0.04
Fe I	5397.13	0.92	− 1.98	eqw	5.31	0.08
Fe I	5405.77	0.99	− 1.85	eqw	5.32	0.08
Fe I	5410.91	4.47	0.4	eqw	5.08	0.04
Fe I	5415.2	4.39	0.64	eqw	5.12	0.04
Fe I	5429.7	0.96	− 1.88	eqw	5.34	0.08
Fe I	5434.52	1.01	− 2.13	eqw	5.34	0.08
Fe I	5497.52	1.01	− 2.82	eqw	5.25	0.07
Fe I	5501.47	0.96	− 3.05	eqw	5.38	0.07
Fe I	5506.78	0.99	− 2.79	eqw	5.33	0.07
Fe I	5569.62	3.42	− 0.52	eqw	5.12	0.05
Fe I	5586.76	3.37	− 0.11	eqw	5.08	0.05
Fe I	5624.54	3.42	− 0.76	eqw	5.08	0.05
Fe I	5662.52	4.18	− 0.41	eqw	5.04	0.04
Fe I	6003.01	3.88	− 1.1	eqw	5.35	0.04
Fe I	6136.61	2.45	− 1.41	eqw	5.28	0.06
Fe I	6137.69	2.59	− 1.35	eqw	5.14	0.06
Fe I	6191.56	2.43	− 1.42	eqw	5.15	0.06
Fe I	6230.72	2.56	− 1.28	eqw	5.27	0.06
Fe I	6246.32	3.6	− 0.77	eqw	5.2	0.05
Fe I	6252.56	2.4	− 1.77	eqw	5.24	0.06
Fe I	6393.6	2.43	− 1.58	eqw	5.28	0.06
Fe I	6411.65	3.65	− 0.59	eqw	5.2	0.05
Fe I	6421.35	2.28	− 2.01	eqw	5.34	0.06
Fe I	6430.85	2.18	− 1.95	eqw	5.28	0.06
Fe I	6494.98	2.4	− 1.24	eqw	5.23	0.06
Fe I	6677.99	2.69	− 1.42	eqw	5.31	0.06
Fe I	7495.07	4.22	− 0.1	eqw	5.23	0.04
Fe II	2424.39	2.58	− 0.94	syn	5.2	0.04
Fe II	2428.8	3.89	− 0.31	syn	5.0	0.07
Fe II	2434.24	5.29	0.25	syn	5.0	0.08
Fe II	2437.65	5.2	− 0.36	syn	5.1	0.08
Fe II	2439.3	3.15	0.45	syn	4.88	0.08
Fe II	2444.51	2.58	0.3	syn	5.2	0.06
Fe II	2445.57	2.7	0.05	syn	4.84	0.08
Fe II	2458.97	3.89	− 0.04	syn	4.9	0.08
Fe II	2461.28	3.23	0.23	syn	5.12	0.08
Fe II	2461.86	3.22	0.34	syn	4.95	0.08
Fe II	2463.28	3.15	− 0.19	syn	5.11	0.1
Fe II	2465.91	3.22	− 0.05	syn	5.1	0.08
Fe II	2472.61	5.55	0.47	syn	5.2	0.08
Fe II	2503.87	3.77	0.32	syn	5.19	0.12
Fe II	2572.97	2.89	− 1.2	syn	5.3	0.09
Fe II	2587.95	4.15	0.23	syn	5.15	0.07
Fe II	2664.66	3.39	0.31	syn	5.15	0.08
Fe II	2718.64	6.22	0.02	syn	5.15	0.06
Fe II	2892.83	1.08	− 2.7	syn	5.2	0.03
Fe II	2944.39	1.7	− 0.85	syn	5.24	0.09
Fe II	2984.82	1.67	− 0.45	syn	5.15	0.08
Fe II	2985.55	1.72	− 0.89	syn	5.12	0.07
Fe II	4173.45	2.58	− 2.38	eqw	5.28	0.03
Fe II	4178.86	2.58	− 2.51	eqw	5.2	0.03
Fe II	4233.16	2.58	− 2.02	eqw	5.26	0.04
Fe II	4385.38	2.78	− 2.64	eqw	5.2	0.03
Fe II	4416.82	2.78	− 2.57	eqw	5.14	0.03
Fe II	4491.41	2.86	− 2.71	eqw	5.17	0.03
Fe II	4508.28	2.86	− 2.42	eqw	5.29	0.03
Fe II	4515.34	2.84	− 2.6	eqw	5.35	0.03
Fe II	4555.89	2.83	− 2.4	eqw	5.23	0.03
Fe II	4576.34	2.84	− 2.95	eqw	5.22	0.03

Table A1 – *continued*

Species	Wavelength (Å)	χ (eV)	log gf	Type	log ϵ(X)	σ_{sys}
Fe II	4583.83	2.81	− 1.94	eqw	5.26	0.03
Fe II	5197.58	3.23	− 2.22	eqw	5.23	0.03
Fe II	5234.63	3.22	− 2.18	eqw	5.19	0.03
Fe II	5276.0	3.2	− 2.01	eqw	5.2	0.03
Co I	2316.85	0.17	− 1.15	syn	2.95	0.14
Co I	3405.12	0.43	0.29	syn	2.98	0.09
Co I	3409.18	0.51	− 0.22	syn	2.76	0.1
Co I	3433.04	0.63	− 0.18	syn	2.84	0.08
Co I	3449.17	0.58	− 0.12	syn	2.75	0.1
Co I	3449.44	0.43	− 0.48	syn	2.87	0.09
Co I	3489.4	0.92	0.18	syn	2.64	0.05
Co I	3513.48	0.1	− 0.79	syn	3.09	0.07
Co I	3529.03	0.17	− 0.89	syn	2.96	0.08
Co I	3995.31	0.92	− 0.18	syn	2.87	0.05
Co I	4121.32	0.92	− 0.33	syn	2.94	0.06
Co II	2311.6	0.56	0.32	syn	2.55	0.1
Co II	2326.14	0.57	− 0.42	syn	2.7	0.03
Co II	2330.36	0.61	− 0.51	syn	2.8	0.06
Co II	2361.52	0.64	− 1.16	syn	2.65	0.13
Co II	2393.91	0.57	− 0.37	syn	2.6	0.12
Co II	2414.07	0.57	− 0.37	syn	2.6	0.06
Co II	2417.66	0.5	− 0.25	syn	2.49	0.09
Co II	2464.2	1.22	− 0.4	syn	2.57	0.35
Co II	2564.0	1.33	0.03	syn	2.55	0.0
Ni I	2441.82	0.21	− 1.51	syn	3.95	0.07
Ni I	2984.13	0.0	− 1.5	syn	3.8	0.13
Ni I	2992.59	0.02	− 1.22	syn	4.0	0.1
Ni I	3423.71	0.21	− 0.71	eqw	4.0	0.16
Ni I	3433.56	0.03	− 0.67	eqw	3.96	0.17
Ni I	3437.28	0.0	− 1.2	eqw	3.93	0.13
Ni I	3452.89	0.11	− 0.9	eqw	4.34	0.18
Ni I	3472.54	0.11	− 0.79	eqw	3.8	0.14
Ni I	3483.78	0.27	− 1.11	eqw	3.75	0.1
Ni I	3492.96	0.11	− 0.24	eqw	4.0	0.19
Ni I	3500.85	0.17	− 1.27	eqw	4.1	0.12
Ni I	3524.54	0.03	0.01	eqw	4.01	0.19
Ni I	3566.37	0.42	− 0.24	eqw	3.83	0.17
Ni I	3597.7	0.21	− 1.1	eqw	4.08	0.14
Ni I	3783.53	0.42	− 1.4	eqw	3.97	0.08
Ni I	3807.14	0.42	− 1.23	eqw	3.92	0.09
Ni I	4604.99	3.48	− 0.24	eqw	4.02	0.04
Ni I	4648.65	3.42	− 0.09	eqw	3.88	0.04
Ni I	4714.42	3.38	0.25	eqw	3.94	0.04
Ni I	5080.53	3.65	0.32	eqw	3.56	0.04
Ni I	5476.9	1.83	− 0.78	eqw	3.9	0.06
Ni II	2297.49	1.32	− 0.33	syn	3.98	0.18
Ni II	2350.85	1.68	− 2.28	syn	3.92	0.17
Ni II	2356.40	1.86	− 0.83	syn	3.91	0.07
Ni II	2415.0	1.86	0.13	syn	4.0	0.0
Ni II	2437.0	1.68	− 0.33	syn	3.91	0.04
Zn I	4722.15	4.03	− 0.37	syn	2.31	0.04
Zn I	4810.53	4.08	− 0.15	syn	2.33	0.04
Ge I	3039.07	0.88	− 0.07	syn	1.4	0.17
As I	2288.11	1.35	− 0.06	syn	<0.84	–
Rb I	7947.6	0.0	− 0.16	syn	<2.42	–
Sr II	4077.71	0.0	0.15	syn	1.01	0.18
Sr II	4215.52	0.0	− 0.17	syn	1.1	0.18
Y II	2422.19	0.41	− 0.08	syn	0.58	0.06
Y II	3549.0	0.13	− 0.29	syn	0.47	0.06
Y II	3600.73	0.18	0.34	syn	0.6	0.08
Y II	3611.04	0.13	0.05	syn	0.28	0.05

Table A1 – *continued*

Species	Wavelength (Å)	χ (eV)	log gf	Type	log ϵ(X)	σ_{sys}
Y II	3950.35	0.1	− 0.73	syn	0.5	0.05
Y II	3982.59	0.13	− 0.56	syn	0.43	0.06
Y II	4235.73	0.13	− 1.27	syn	0.65	0.03
Y II	4398.01	0.13	− 0.75	syn	0.45	0.07
Y II	4883.68	1.08	0.19	syn	0.24	0.04
Y II	5205.72	1.03	− 0.28	syn	0.55	0.06
Zr II	2567.64	0.0	− 0.17	syn	0.99	0.04
Zr II	2700.13	0.1	− 0.08	syn	1.05	0.0
Zr II	2745.85	0.10	− 0.31	syn	1.19	0.02
Zr II	2758.81	0.0	− 0.56	syn	1.12	0.22
Zr II	2915.99	0.47	− 0.5	syn	1.12	0.1
Zr II	3430.53	0.47	− 0.16	syn	1.15	0.0
Zr II	3505.67	0.16	− 0.39	syn	1.2	0.05
Zr II	3551.95	0.1	− 0.36	syn	1.24	0.07
Zr II	3998.96	0.56	− 0.52	syn	1.1	0.05
Zr II	4149.2	0.8	− 0.04	syn	1.07	0.05
Zr II	4156.23	0.71	− 0.78	syn	1.0	0.06
Zr II	4161.2	0.71	− 0.59	syn	1.2	0.06
Zr II	4208.98	0.71	− 0.51	syn	1.15	0.05
Zr II	4359.73	1.24	− 0.51	syn	1.25	0.09
Zr II	4496.96	0.71	− 0.89	syn	1.19	0.05
Nb II	2927.81	0.51	0.16	syn	<0.93	–
Mo II	2871.51	1.54	0.06	syn	0.75	0.05
Ru II	2456.0	1.35	0.06	syn	<1.54	–
Rh I	3434.89	0.0	0.44	syn	<1.52	–
Pd I	3404.58	0.81	0.32	syn	<1.34	–
Ag I	3382.89	0.0	− 0.33	syn	<1.38	–
Cd I	2288.02	0.0	0.11	syn	0.63	0.13
In II	2306.06	0.0	− 2.3	syn	<0.83	–
Sn I	2286.68	0.42	− 0.94	syn	<2.94	–
Te I	2385.79	0.59	− 0.81	syn	<1.83	–
Ba II	4554.03	0.0	0.17	syn	0.55	0.07
Ba II	4934.08	0.0	− 0.16	syn	0.4	0.07
Ba II	5853.68	0.6	− 0.91	syn	0.47	0.03
Ba II	6141.71	0.7	− 0.08	syn	0.5	0.06
Ba II	6496.9	0.6	− 0.38	syn	0.47	0.04
La II	3949.1	0.4	0.49	syn	−0.2	0.06
La II	3988.51	0.4	0.21	syn	−0.2	0.06
La II	4077.34	0.24	− 0.06	syn	−0.05	0.07
La II	4086.71	0.0	− 0.07	syn	−0.18	0.05
La II	4123.22	0.32	0.13	syn	−0.16	0.06
Ce II	4460.21	0.48	0.28	syn	0.22	0.02
Ce II	4562.36	0.48	0.21	syn	0.25	0.07
Pr II	4225.32	0.0	0.32	syn	−0.4	0.2
Nd II	3900.22	0.47	0.1	syn	0.3	0.12
Nd II	4012.24	0.63	0.81	syn	0.07	0.19
Nd II	4109.45	0.32	0.35	syn	0.03	0.07
Nd II	4156.08	0.18	0.16	syn	0.1	0.07
Nd II	4177.32	0.06	− 0.1	syn	0.34	0.09
Nd II	4303.57	0.0	0.08	syn	0.17	0.13
Sm II	4329.02	0.18	− 0.51	syn	0.18	0.07
Eu II	3819.67	0.0	0.51	syn	−0.51	0.04
Eu II	3907.11	0.21	0.17	syn	−0.41	0.04
Eu II	4129.72	0.0	0.22	syn	−0.47	0.03
Eu II	4205.04	0.0	0.21	syn	−0.44	0.04
Eu II	4435.58	0.21	− 0.11	syn	−0.45	0.11
Gd II	3032.84	0.08	0.3	syn	0.4	0.19
Gd II	4063.38	0.99	0.33	syn	0.4	0.18
Gd II	4251.73	0.38	− 0.22	syn	0.35	0.07
Tb II	3874.17	0.0	0.27	syn	<−0.06	–
Dy II	3407.8	0.0	0.18	syn	0.3	0.09

Table A1 – *continued*

Species	Wavelength (Å)	χ (eV)	log gf	Type	log ϵ(X)	σ_{sys}
Dy II	3531.71	0.0	0.77	syn	0.32	0.19
Dy II	3757.37	0.1	− 0.17	syn	0.37	0.06
Dy II	3944.68	0.0	0.11	syn	0.17	0.04
Dy II	4077.97	0.1	− 0.04	syn	0.15	0.05
Ho II	3456.01	0.0	0.76	syn	−0.42	0.07
Ho II	4045.45	0.0	− 0.05	syn	−0.3	0.07
Er II	3499.1	0.06	0.29	syn	0.22	0.07
Er II	3906.31	0.0	0.12	syn	0.01	0.12
Tm II	3848.02	0.0	− 0.14	syn	−0.67	0.06
Yb II	3694.19	0.0	− 0.3	syn	−0.27	0.05
Lu II	2615.41	0.0	0.11	syn	−0.7	0.17
Hf II	3399.79	0.0	− 0.57	syn	<0.67	–

Table A1 – *continued*

Species	Wavelength (Å)	χ (eV)	log gf	Type	log ϵ(X)	σ_{sys}
Os II	2282.28	0.0	− 0.57	syn	0.49	0.29
Ir I	2639.71	0.0	− 0.31	syn	<1.01	–
Pt I	2659.45	0.0	− 0.03	syn	0.53	0.1
Pt I	2997.96	0.10	− 0.50	syn	0.68	0.16
Au I	2427.95	0.0	− 0.15	syn	−0.1	0.12
Au I	2675.95	0.0	− 0.45	syn	−0.02	0.11
Th II	4019.13	0.0	− 0.23	syn	<−0.38	–
C-H	4313.0	–	–	syn	6.7	0.12
C-N	3875.0	–	–	syn	<7.73	–

This paper has been typeset from a TEX/LATEX file prepared by the author.